remote sensing

Article

Petrological and Mineralogical Characteristics of Exposed Materials on the Floors of the Lavoisier and Surrounding Craters

Eung Seok Yi [1], Kyeong Ja Kim [2,*], Christian Wöhler [3], Alexey A. Berezhnoy [4,5], Yong Ha Kim [1] and Seulgi Moon [6]

1 Department of Astronomy, Space Science, and Geology, Chungnam National University, Daejeon 34134, Korea
2 Geological Research Center, Geology Division, Korea Institute of Geoscience and Mineral Resources, 124, Gwahak-ro, Yuseong-gu, Daejeon 34132, Korea
3 Image Analysis Group, TU Dortmund University, Otto-Hahn-Straße 4, 44227 Dortmund, Germany
4 Sternberg Astronomical Institute, Moscow State University, Universitetskij Pr., 13, 119234 Moscow, Russia
5 Institute of Physics, Kazan Federal University, Kremlyovskaya Str., 18, 420008 Kazan, Russia
6 Earth, Planetary & Space Sciences, University of California, Los Angeles, CA 90095-1567, USA
* Correspondence: kjkim@kigam.re.kr

Abstract: Five floor-fractured craters (FFCs), Lavoisier crater and four craters surrounding it (Lavoisier C, Lavoisier E, Lavoisier F, and Lavoisier H), are distributed along the boundary between the northwestern part of the Oceanus Procellarum and the highlands. This study examines the uplifted or exposed materials on the fractured floors of these five impact craters using petrological, mineralogical, and morphological analyses. We inferred the processes that uplifted or exposed the materials from the subsurface to the crater floor using the Chandrayaan-1 Moon Mineralogy Mapper (M^3) level 1b (thermally and topographically corrected spectral radiance) data and level 2 (spectral reflectance) data. The elemental abundances, petrological, and mineralogical characteristics of the study regions were mapped. We confirm that mare basalts and dark mantle deposits exist on the floors of these five craters. These two materials (mare basalts and dark mantle deposits) were used to identify minerals exposed on the floor surface of craters using spectral reflectance spectra. Two mineral groups were identified: pigeonite (or orthopyroxene in norite (low-Ca pyroxene) occurred in the craters Lavoisier, Lavoisier F, and Lavoisier H, and subcalcic augite (high-Ca pyroxene) occurs in the craters Lavoisier C and E. Our approach demonstrates that the characterization of uplifted or exposed surface minerals using elemental maps, spectral parameter composite maps, and reflectance spectra can provide information critical for prospective studies involving lunar geology and in situ resource utilization.

Keywords: the Moon; mare basalt; Mg-suite rock; floor-fractured crater; petrological analysis; mineralogical analysis

check for updates

Citation: Yi, E.S.; Kim, K.J.; Wöhler, C.; Berezhnoy, A.A.; Kim, Y.H.; Moon, S. Petrological and Mineralogical Characteristics of Exposed Materials on the Floors of the Lavoisier and Surrounding Craters. *Remote Sens.* **2022**, *14*, 4313. https://doi.org/10.3390/rs14174313

Academic Editors: Roberto Orosei and Kaichang Di

Received: 12 July 2022
Accepted: 24 August 2022
Published: 1 September 2022

1. Introduction and Background

Lavoisier and its four neighboring craters are located in the boundary region between the northwestern part of the Oceanus Procellarum and highlands on the lunar surface. They include lunar floor-fractured craters (FFCs), mare basalts, and dark mantle deposits (DMDs). An FFC is defined as a crater whose floor has been uplifted and fractured in an anomalous and irregular way. FFCs have also been detected on Venus, Mars, and Ceres [1–3]. The distribution of FFCs was described in detail by Schultz (1976) [4], and viscous relaxation was first mentioned by Masursky (1964) [5] and Daneš (1965) [6] as a possible formation mechanism. The first of two mechanisms by which FFCs can be formed are uplifting of the crater floor caused by shallow magmatic intrusion and sill formation [7–9]. Second, the crater floor is split by fractures because of thermally driven viscous relaxation [10].

The materials to make the path (caldera, dike, diapir, etc.) could be residues left by a lunar magma ocean (LMO). If all of the Moon melted after it formed, accumulated materials (described as Mg-rich and Fe-rich) from the lunar upper mantle in the lunar magma ocean state would be produced by the gravitational restructuring and would stay in the potassium (K) and rare-earth elements and phosphorus (KREEP) layer [11–14]. Then, the materials would be mixed with different types of plagioclases and Mg-rich olivine and form diapirs [13,15].

Most of the FFCs found in the entire boundaries of the highlands and mare have been examined in preliminary investigations [16–19]. The aim of this study is to focus on the northwestern part of the largest mare area on the lunar surface, Oceanus Procellarum. The uplifted or exposed materials from the subsurface (DMDs, mixed mare basalts with impact-melt materials) were identified in FFCs using petrological analysis and infrared spectroscopic techniques in previous studies [7,9,20]. Previous studies commented that the mare basalts and the dark mantle deposits have similar characteristics (e.g., spectra—absorption features [16–18]). They said the two materials are difficult to distinguish using the spectrum characteristics. We tried to distinguish the mare basalts and the dark mantle deposits using the spectra characteristics and referred to the previous studies (e.g., Adams, 1974—absorption features, band centers). In addition, we focused to the process of uplifted or exposed materials from the subsurface to the lunar crater floor. The evolution process for the uplifted or exposed materials from the subsurface onto the lunar surface is important. In particular, according to Nakamura et al. [15], the low-calcium pyroxene (LCP: e.g., pigeonite (Ca,Mg,Fe)(Mg,Fe)Si_2O_6), etc.) regions were thought to be materials on the crater floor exposed and showing through parts of the lunar upper mantle [21] and the highland crust. These materials can be measured using infrared spectroscopic techniques. The spectra are determined by wavelengths intrinsic to the crystal structure of these minerals [22,23]. Low-Ca pyroxene is distributed in the composition range of a ternary diagram formed by the abundances of Ca, Mg, and Fe in the pyroxene minerals. In 'low-Ca pyroxene (e.g., pigeonite)', the Ca content is 5–20%. In 'high-Ca pyroxene (e.g., augite (Ca,Na)(Mg,Fe,Al,Ti)$(Si,Al)_2O_6$)', the Ca content is 20–45%. Subcalcic augite has a lower Ca content than augite [24]. Clinopyroxenes are divided into low-Ca pyroxene and high-Ca pyroxene. In orthopyroxenes, the Ca contents is less than 5%. The main minerals of the orthopyroxene group are enstatite ($MgSiO_3$) and ferrosilite ($FeSiO_3$) [24–26]. Minerals like low-calcium pyroxenes (LCP) are also found in other regions of the Moon such as at the boundary of Mare Imbrium [15]. The exposed materials can be investigated in the mapping using petrological and the elemental abundances analysis [27–29].

In this study, we characterized the uplifted or exposed materials from the subsurface in FFCs on the northwestern boundary of the Oceanus Procellarum. The study areas are five craters (Lavoisier, Lavoisier C, Lavoisier E, Lavoisier F, and Lavoisier H craters) (Figure 1).

We used the United States Geological Survey geological map [30] to investigate geological features of the five craters in the study area (right image in Figure 1). The craters Lavoisier and Lavoisier F commonly have pre-Nectarian crater (pNc) and Imbrian Plains (Ip) materials [31]. The craters Lavoisier C and Lavoisier E commonly have Imbrian mare upper (Im2) material. Thus, the FFCs in the study area were formed from the pre-Nectarian to the Imbrian age period [30].

We estimated the presence of mare basalts and Mg-suite rock in these craters and examined how they were exposed at the surface using petrological, mineralogical, and morphological analyses. To do this, we investigated the mixed materials based on their spectral signature for the main rock types [32,33] and referred to the USGS Digital Unified Global Geologic Map of the Moon [30], spectral parameter maps, and petrological false-color composites derived from Chandrayaan-1 Moon Mineralogy (M^3) data [28,34–36]. Then, we examined the spectra) using multispectral analysis for the study area. Finally, by adding a digital elevation model (DEM) and topographic profile data analysis, we examined how the materials (DMDs and materials mixed by impacts) were exposed on the crater floors.

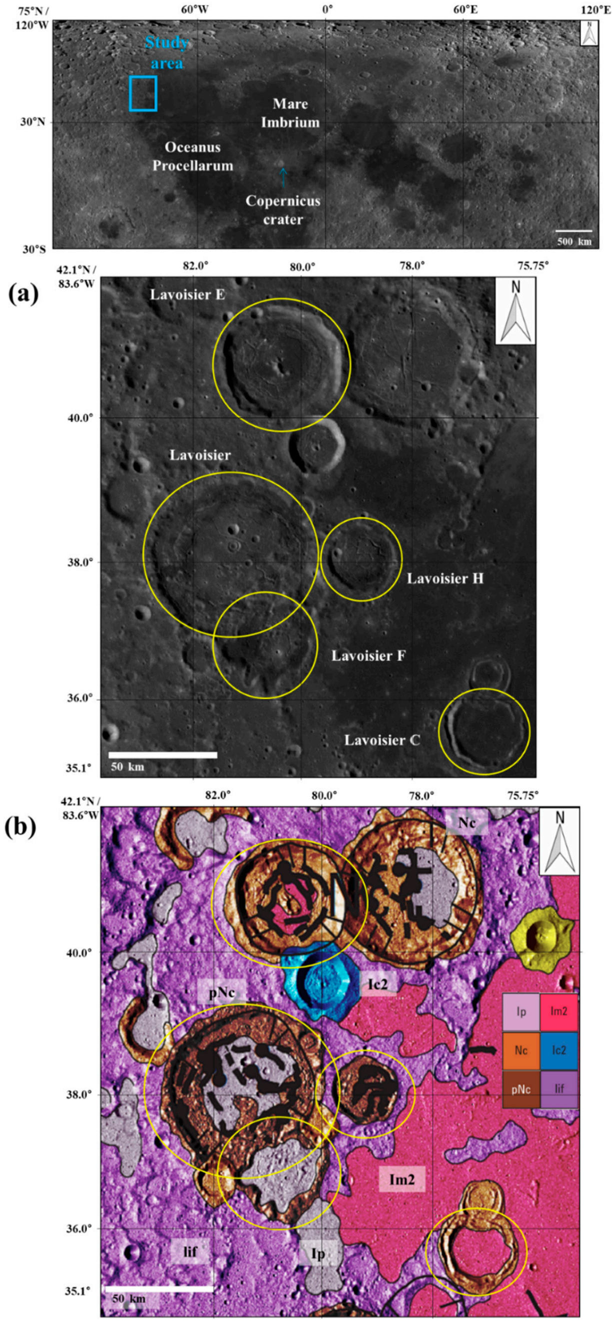

Figure 1. (**a**) Wide-angle camera (WAC) base map mosaic (**a**) showing the distribution of FFCs and mare basalts in the research area. The blue boxed area (study area, upper (**a**)) is marked in the northwestern edge of Oceanus Procellarum. The yellow circles have the FFCs that include the mare basalts (the data were downloaded from https://quickmap.lroc.asu.edu, accessed on 1 April 2022). The geological map (**b**) referred from the United States Geological Survey (USGS) shows the materials for each crater; The Lavoisier E-Nc, Im2, Lavoisier and Lavoisier F-pNc, Nc, Ip, Lavoisier H-pNc, Lavoisier C-Nc, Im2. The explanation about the materials follow as the USGS geological units; pre-Nectarian crater (pNc, pre-Nectarian: −4.5 to −3.9 Ga), Nectarian crater (Nc, Nectarian: −3.9 to −3.8 Ga), Imbrian Plains (Ip, impact crater ejecta, Imbrian: −3.8 to −3.2 Ga), Imbrian mare, upper (Im2, upper mare material, basaltic lava flows), Imbrian Crater, Upper (Ic2, materials of the Orientale group), Imbrian Imbrium Fra Mauro Formation (Iif, surface texture locally hummocky.). We adopted a part of the USGS Digital Unified Global Geologic Map of the Moon [30], https://astrogeology.usgs.gov/search/map/Moon/Geology/Unified_Geologic_Map_of_the_Moon_GIS_v2, accessed on 3 April 2021. The list for the center position of each crater is presented in the Appendix A.

2. Methods and Datasets

To carry out a study of the mafic materials (Mg-suite rock) associated with the floor-fractured craters (FFCs), we needed to analyze spectral parameter maps and petrological RGB composites inferred from M^3 data [37]. Appendix B shows a flow chart of the crater investigation in this study.

2.1. Petrological Method

The petrological method uses estimates of the relative abundances of the main rock types of the Moon (i.e., mare basalts, Mg-rich rocks, and ferroan anorthosite) based on the Mg and Fe elemental abundances [27]. For estimating the abundances of Mg and Fe, we computed parameters describing the mafic absorption bands at ~1000 nm and ~2000 nm in the M^3 reflectance spectra and used a multivariate regression technique based on Lunar Prospector gamma-ray spectrometer (LP GRS) data [28,36,38]. The estimation of rock types was based on the method of Berezhnoy et al. [27], who compared LP GRS data [39,40] at 50 and 150 km above the ground with the bulk composition of samples returned from the surface [41,42].

The M^3 radiance data were corrected for thermal emission [34,35] by taking into account the effect of a rough regolith surface (slope of 9 degrees). Topographic effects were removed based on a high-resolution DEM [28,43] obtained by combining the shape from shading and GLD100 stereo data [44]. Relying on the Hapke model [45,46], the spectral reflectances were normalized to a uniform illumination and observation geometry of 30° incidence angle and 0° emission angle [28]. These calibrated reflectance spectra were used for extracting spectral parameters and estimating the abundances of Mg, Fe, and Ti and the relative fractions of mare basalt, Mg-rich rock and feldspathic material [27,28,36].

The rock fractions were derived from a ternary diagram denoting the Mg-Fe space [27] and are visualized in this study as false-color RGB composites with the R, G, and B channels indicating the mare basalt, Mg-rich rock and feldspathic rock fraction, respectively. The "Mg-rich rock" from our spectral analysis of the Lavoisier region consists of mafic Mg-suite materials such as norite containing orthopyroxene ($(Mg,Fe,Ca)(Mg,Fe,Al)(Si,Al)_2O_6$), rather than olivine ($(Mg^{2+},Fe^{2+})_2SiO_4$) or Mg-spinel $MgAl_2O_4$.

The method used in this study for estimating the abundances of the key elements Mg, Fe, and Ti has been examined extensively by Wöhler et al. [47] and Bhatt et al., [36] with respect to its accuracy. An indicator of the (internal) accuracy of the regression function is the confidence interval, which is a measure of the spread of the probability distribution of the fitted regression models, given the amount of noise present in the data. For our fitted regression models, the confidence interval on the 95% significance level is always well below 1 wt% for the examined elements. Furthermore, the elemental abundances estimated by the regression model were compared in Bhatt et al. [36] to laboratory measurements conducted on returned Apollo and Luna samples. The corresponding root-mean-square deviations are in the range of 1–2 wt%, where the regression function does not exhibit systematic deviations from the landing-site-specific laboratory measurements. Hence, we can safely assume that the regression-based technique employed in this study is able to infer elemental abundance values from M^3 reflectance spectra at an accuracy that is sufficient to distinguish between mare basalts, Mg-rich materials, and feldspathic materials with a spatial resolution of a few hundred meters.

2.2. Mineralogical Method and Multispectral Analysis

We performed a mineralogical analysis to verify the presence of mare basalts using false-color composites inferred from the M^3 level 2 data [37]. We used the ENVI (Environment for Visualizing Images) software and the integrated band depth (IBD) method to investigate the mineral distribution. The method to provide the false-color composites and the technique to create the spectra (see Figure 2 and Equations (1) and (2) below) have been used in a variety of recent publications regarding the distribution of minerals on the lunar surface (e.g., Öhman et al. [48]; Grumpe et al. [49]). The derived spectral parameters are stored as RGB images, where the color channels are defined as follows: red: IBD1000 (integrated band depth of the mafic absorption band around 1000 nm); green: IBD2000 (integrated band depth of the mafic absorption band around 2000 nm); and blue: reflectance at 1578 nm [50].

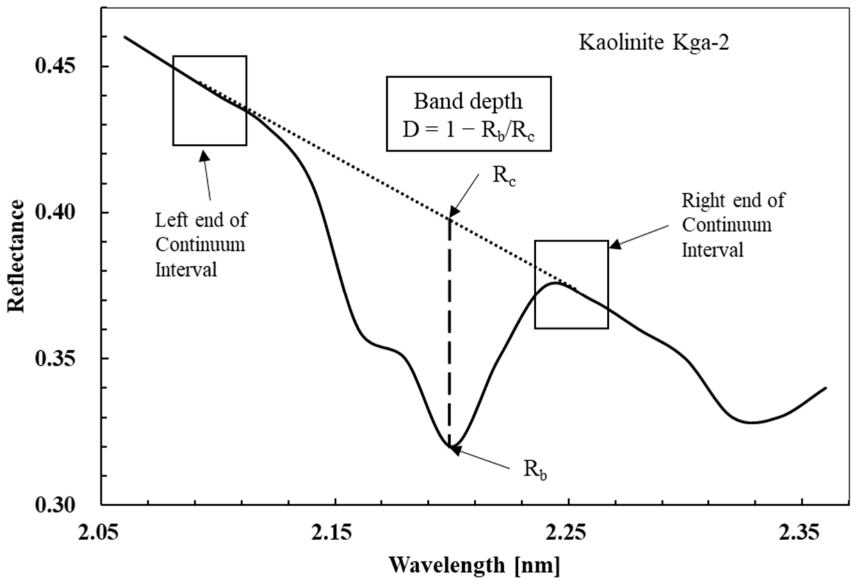

Figure 2. Example showing the characteristics of absorption features. Figure modified from Clark et al. (2003) [51].

Figure 2 displays the properties of an absorption band. The R_b value is the reflectance at the band center (maximum absorption band). The term R_c is the modeled linear continuum, and the point where the extension line of R_b meets the line between the left and right continuum intervals is shown with an arrow in Figure 2. The band depth (BD) means the length from R_b to the corresponding R_c. The integrated band depth (IBD) is the integral of the BD in Figure 2 [51]. The IBD1000 and IBD2000 parameters are calculated as follows:

$$\text{IBD1000} = \sum_{n=0}^{26}\left(1 - \frac{R(789+20n)}{R_c(789+20n)}\right) \quad (1)$$

$$\text{IBD2000} = \sum_{n=0}^{21}\left(1 - \frac{R(1658+40n)}{R_c(1658+40n)}\right) \quad (2)$$

In Equations (1) and (2), R is the spectral reflectance and R_c is the modeled linear continuum. The lower and upper limits of the integration are chosen such that they cover the complete absorption band for the relevant mineral species. The absorption feature at 1578 nm in the continuum-removed reflectance represents highlands with weak mafic absorption [50].

False-color (RGB) composites constructed in this way can reveal the overall mineral distribution qualitatively [48]. Pyroxene (including high-calcium clinopyroxene ((Ca,Mg,Fe,Na)-(Mg,Fe,Al)(Si,Al)$_2$O$_6$) and low-calcium orthopyroxene) has absorption bands at 900–1050 nm and 1800–2300 nm [52]. Olivine (Mg,Fe)$_2$SiO$_4$ has its main absorption band near 1000 nm and no absorption band at 2000 nm. Clinopyroxene, low-calcium pyroxene, and rare Mg-spinel MgAl$_2$O$_4$ all have absorption bands near 2000 nm [53]. Here, large values of IBD1000 indicate the presence of pyroxene and/or olivine, and large values of IBD2000 also indicate pyroxene, in particular low-Ca pyroxene.

Spectroscopic investigation can help in efforts to identify mare basalt components. The RGB composite using IBD1000 and IBD2000 can be used to observe the mineral distribution and to recognize exposed materials (e.g., DMDs, mare basalts mixed with impact melt) near the floor-fractured regions. Furthermore, the band center was inferred using the minimum points of the absorption band in the continuum-removed spectra. We compared the band center wavelengths determined in this study to previous works [52].

2.3. Morphological Method

We used the LRO LOLA digital elevation model co-registered with Selene data (SLDEM) and the ArcGIS (ArcMap) software to conduct geological and geomorphological analyses. SLDEM is a dataset combining Japan's SELENE-1 Terrain Camera (TC) Digital Elevation Model (DEM) [54] and NASA's Lunar Reconnaissance Orbiter (LRO) Lunar Orbiter Laser Altimeter (LOLA) elevation model data. This dataset is corrected for the errors in the TC tiles resulting from imperfect knowledge of the SELENE orbit. It is also corrected for errors in camera pointing, focal length, and orbital uncertainties in the offsets in the LOLA profiles, as well as for errors in the laser bore-sight model. The complementary data show a difference of about 3–4 m in vertical accuracy between the co-registered interpolated TC stereo data and the vertical LOLA data. Additionally, the accuracy of the map was increased by matching the DEM-based pseudo-crossovers and LOLA-only crossovers [54]. We used the SLDEM2015 topographic map at a resolution of 512 pixels/degree.

We compared the slope and aspect (azimuth angle of the slopes) analysis for the five craters under study based on the WAC base map (data downloaded from https://quickmap.lroc.asu.edu, accessed on 1 April 2022). Studies of slope and aspect values will be expected to distinguish the relatively flat mare basalts regions, the rough crater floor, and floor-fractured regions. Such analysis can also distinguish the characteristics between the mare basalts regions and the DMDs, which are located near the floor-fractured regions. For example, the floor-fractured regions around the mare basalts and DMDs have different slope values and degrees of roughness comparable to flat regions around the center of Oceanus Procellarum.

3. Results

3.1. Elemental Abundances and Petrological and Mineralogical Results by RGB Composites

3.1.1. Elemental Abundances (Fe, Mg, Ca, and Mg#) and Petrological Results

Figure 3 shows maps using the thermally and photometrically corrected M^3 level 1b data. We constructed maps of elemental abundances of Fe, Mg, Ca, and Mg# (Mg#=Mg/(Mg+Fe)) and petrological maps based on the Mg- and Fe abundances to identify dark mantle deposits (DMDs) and mare basalts in our study area. The Fe, Mg, Ca, and Mg# maps are presented as false-color maps and the petrological Mg-Fe maps are presented in the corresponding RGB composites as follows: red and orange—mare basalts, green—Mg-rich rocks, and blue—anorthosites ($CaAl_2Si_2O_8$). We can distinguish between the mare basalts and the other rocks through the Fe, Mg, Ca, Mg#, and the petrological Mg-Fe maps. The DMDs in the Lavoisier, Lavoisier F, and Lavoisier H crater floors have in common the presence of high-Fe and high-Mg mare basalts. They are interpreted as orthopyroxene commonly found in norite. According to Bhatt et al. [36], the Fe, Mg, and Ca content around the Lavoisier crater is higher than 10 wt%. Our study region is also shown in FeO, MgO, and CaO global maps [55] and maps of mafic mineral abundances [56]. The northern part of the Lavoisier Crater wall consists of relatively high-Fe and low-Mg mare basalts. The DMDs visible in the petrological Mg-Fe map (southern part of Lavoisier H, green) have similar petrological properties as the dark mantle deposits in the craters Lavoisier and Lavoisier F.

The crater floors of Lavoisier E and C exhibit high-Fe and low-Ti mare basalts. The Lavoisier E Crater floor (Figure 3b) apparently has mare basalts and Mg-rich rocks. The materials in the west of the two areas have a lower Mg content than the eastern sides. The map of the floor of Lavoisier C (Figure 3d) shows that the crater floor (orange) has petrological properties similar to those outside the crater in Oceanus Procellarum.

The Ca map of the Lavoisier Crater floor shows strong variations. In particular, the DMDs on the crater floor of Lavoisier F have a low-Ca content (2–6 wt%). The mare basalts on the five crater floors contain 4–8 wt% Ca. The Ca content of the mare basalts on the crater floor of Lavoisier C appears to be similar to the mare basalts outside the crater.

3.1.2. Petrological and Mineralogical Results

The construction of petrological RGB composites is one of the techniques that can be used to interpret spectroscopic data. It is useful for estimating the presence of mare basalts, Mg-rich rocks, and anorthosites in the highlands. In our study area, the presence of mare basalts was confirmed by petrological mappings of the floor-fractured craters.

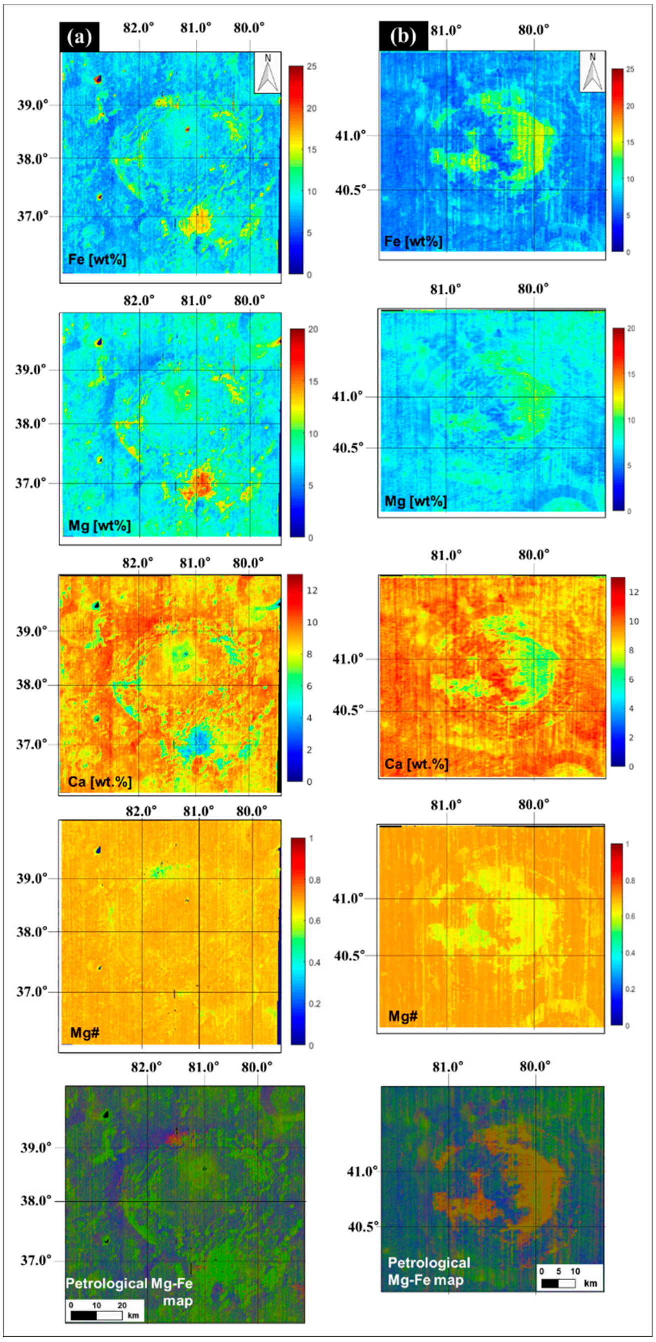

Figure 3. *Cont.*

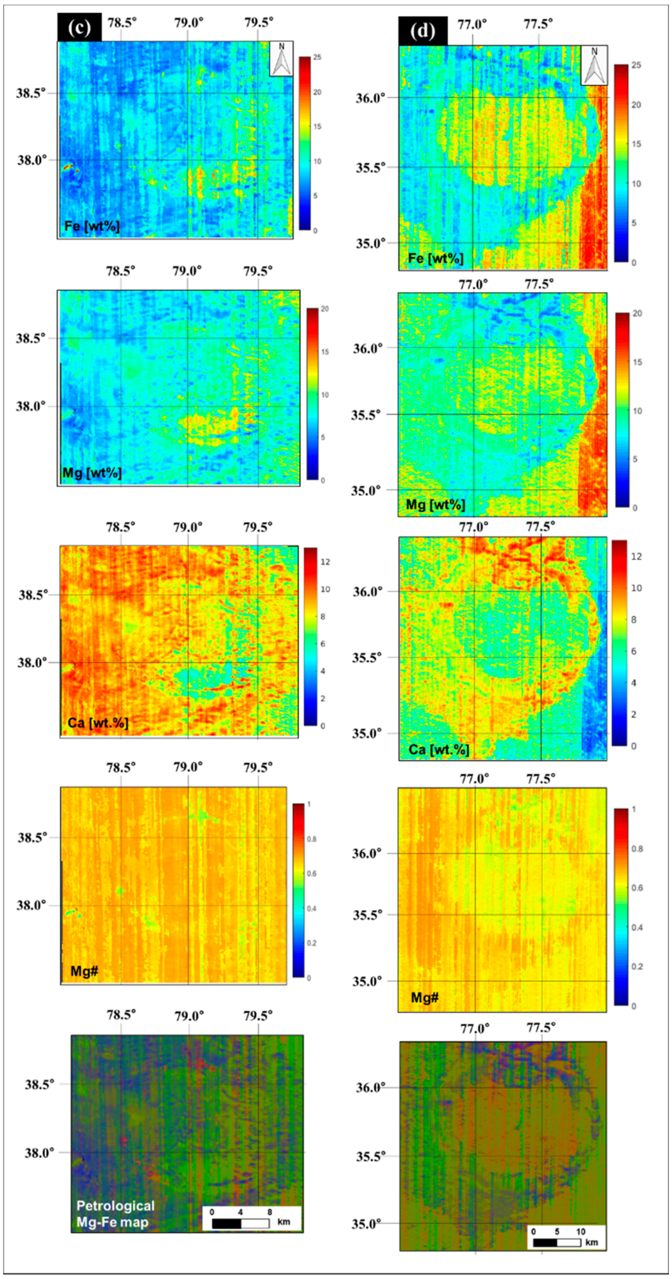

Figure 3. Maps indicating the elemental abundances of Fe, Mg and Ca, the Mg# (Mg/(Mg + Fe)), and the petrological Mg-Fe map in the study area [28,34–36]. The Fe abundance distribution appears from 0 wt% (blue, lowest abundance) to 25 wt% (red, highest abundance). The Mg abundance distribution made of 0 wt% (blue) to 10 wt% (red). The Ca abundance is distributed from 0 wt% (blue) to 12 wt% (red). The Mg# distribution is shown with the same color scale, but the color indices appear from 0 (blue) to 1 (red). In the petrological Mg-Fe map, red and orange denotes mare basalts, green denotes Mg-rich rocks, and blue denotes anorthosite. (**a**) Lavoisier and Lavoisier F, (**b**) Lavoisier E, (**c**) Lavoisier H, (**d**) Lavoisier C. The spatial resolution of the petrological Mg-Fe map is 140 m/pixel.

Based on the approach described above (see also Figure 3) we performed a study of the petrological and mineralogical composition. Figure 4 shows spectral parameter RGB composites using the M^3 level 2 data (left) and the petrological maps obtained based on thermally and topographically corrected M^3 level 1b data (right). DMDs (green arrows in the WAC base map) are apparent on the crater floors of Lavoisier, Lavoisier F, and Lavoisier H as indicated by the green color in the two RGB composites. The deposits occur on the crater floor, including the fractured terrain and in regions between the floor and the wall.

The relatively abundant Mg-rich rock in the middle of the Lavoisier and Lavoisier F crater floors and the western edge of the Lavoisier H floor appears to be excavated by small impact craters. The areas of mixed mare basalts (red) and anorthosites (blue) in Figure 4 (right) appear on the floor, around the crater, and in parts of the wall of Lavoisier, Lavoisier F, and the western wall of the crater Lavoisier H. The western part of the crater wall of Lavoisier C exhibits a mainly feldspathic highland composition with small amounts of intermixed Mg-rich rocks (Figure 4).

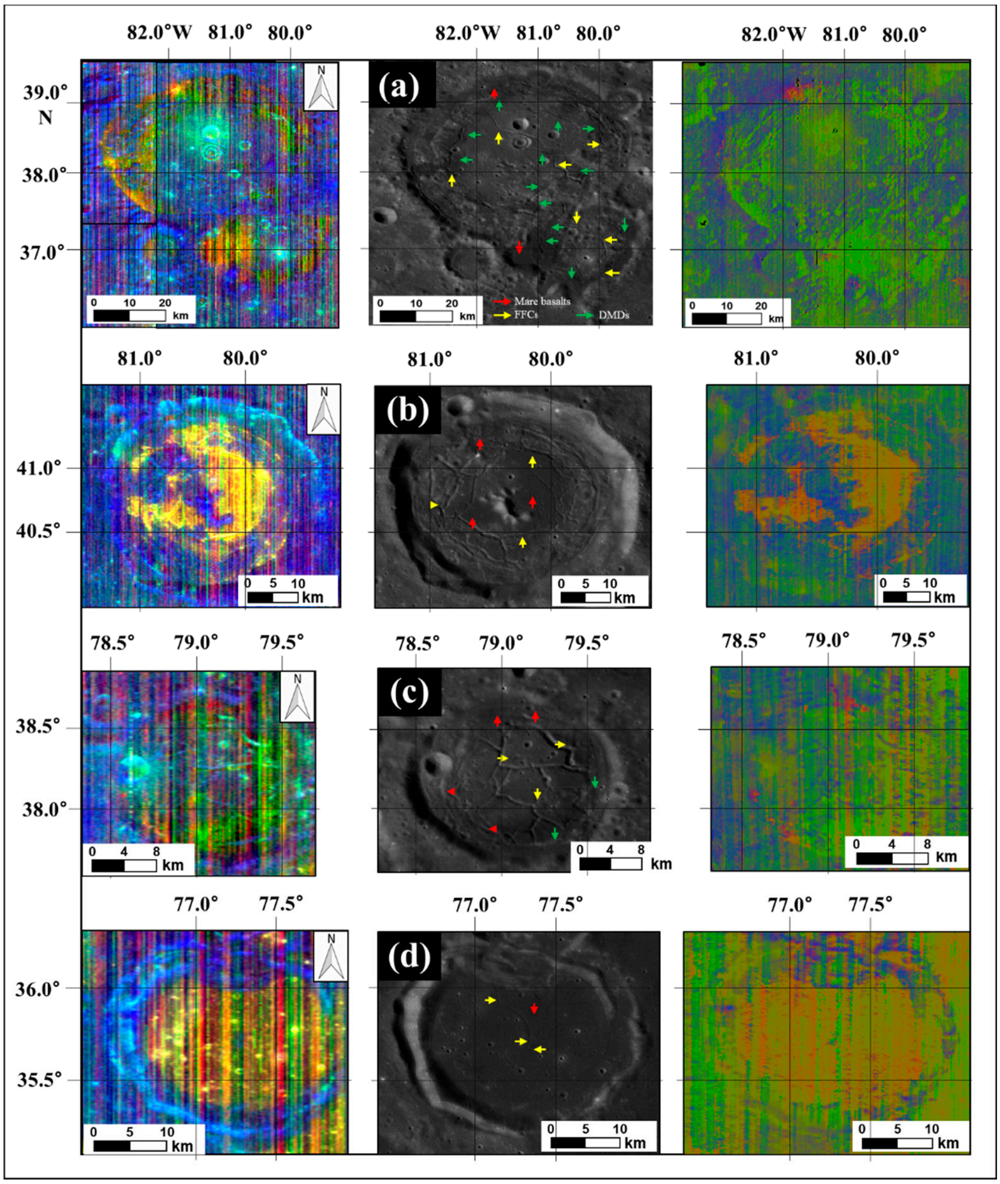

Figure 4. WAC base map (**middle**), mineralogical maps (**left**) using the M^3 level 2 data, and petrological maps obtained based on M^3 level 1b data (**right**) (see [28,34–36]) of the study area. The red arrows indicate the mare basalts in the WAC base map (middle) and the yellow arrows indicate the floor-fractured craters (FFCs). The green arrows correspond to the dark mantle deposits (DMDs) from Souchon et al. [57]. The false colors of the left RGB composites denote the IBD1000 (red), IBD2000 (green), and 1578 nm albedo (blue). The false colors in the right RGB composite correspond to mare basalts (red), Mg-rich rocks (green), and anorthosite (blue). Regions where mare basalts exist are marked by orange or yellow colors in the two RGB composites. (**a**) Lavoisier and Lavoisier F, (**b**) Lavoisier E, (**c**) Lavoisier H, (**d**) Lavoisier C (the data were downloaded from https://quickmap.lroc.asu.edu, accessed on 1 April 2022). The resolution of the maps is 140 m/pixel [37].

The mare basalts (red arrows in the middle column of Figure 4) on the Lavoisier E (b) and Lavoisier C (d) crater floors appear in orange or yellow color in the two RGB composites and are mixed with mare basalts (red channel, IBD1000 in the left column of Figure 4) and Mg-rich rocks (green channel, IBD2000 in the left column of Figure 4). The Lavoisier, Lavoisier F, and Lavoisier H crater floors have small amounts of mare basalts. In previous studies, mare basalts were identified in spectra using mineralogical analysis [32]. According to Besse et al. [32] clinopyroxene and orthopyroxene have strong absorption bands at about 1000 nm and 2000 nm, whereas the 2000 nm absorption is weak or absent in olivine. If these minerals are mixed with high-Ca pyroxene in the rock, the locations of the absorption bands are shifted. This phenomenon is similar to that when mare basalts (red) are mixed with the Ca-containing anorthosites of the highlands (blue) in the RGB composites (purple), or Mg-rich rocks (green) are mixed with anorthosites of the highlands (blue) in the RGB composites (blue-green, crater wall and around the crater).

3.2. Mineralogical Results Obtained by Spectral Reflectance Technique

The reflectance spectra and continuum-removed spectra of Lavoisier and the four surrounding craters are shown in Figures 5–8. The locations from which the reflectance spectra were extracted contain materials indicated as H (highland material), C (crater wall), cF (crater floor), M (mare basalts), and D (dark mantle deposits).

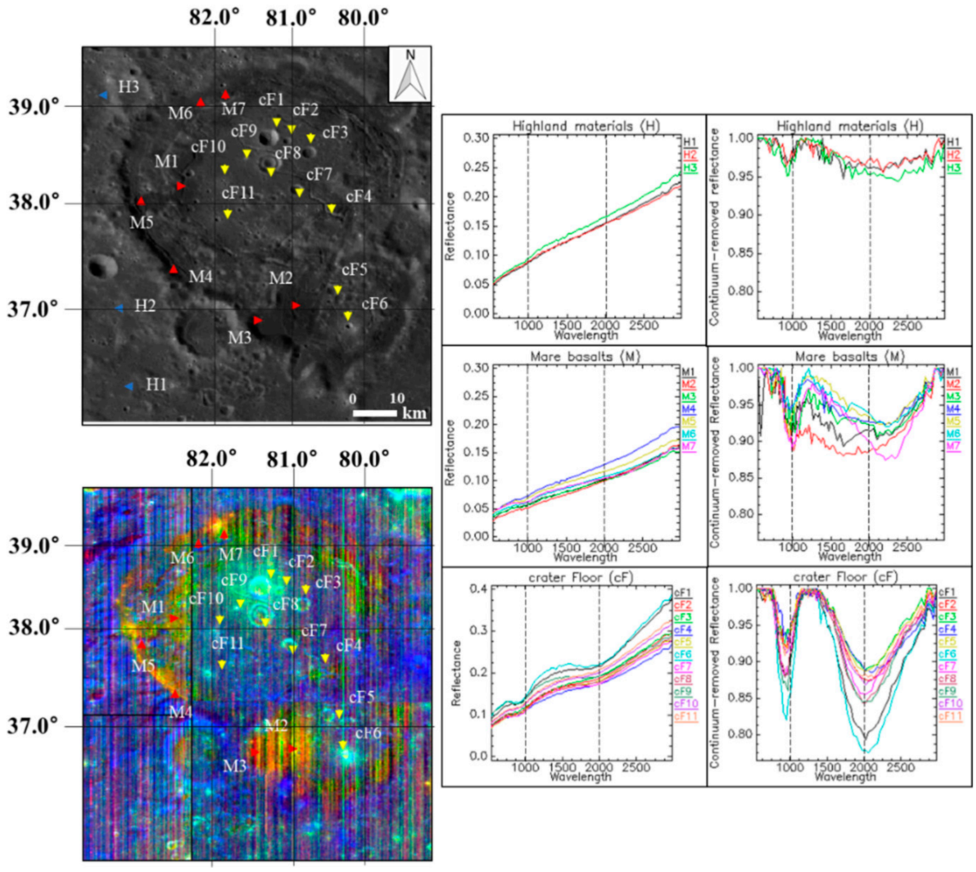

Figure 5. The WAC base map of the craters Lavoisier and Lavoisier F (Figure 4a) shows the locations in highland materials (H1–H3, blue arrows), mare basalts (M1–M7, red arrows), and on the crater floors (cF1–cF11, yellow arrows). To the right, the corresponding reflectance spectra and continuum-removed spectra are shown. On the lower left, the RGB composite derived from the M^3 level 2 data is shown. The dashed lines in the spectra indicate the wavelengths of 1000 nm and 2000 nm. The WAC base map was taken from https://quickmap.lroc.asu.edu, accessed on 1 April 2022. The location of each spectrum in Figure 5 to Figure 8 is provided in the Appendix C.

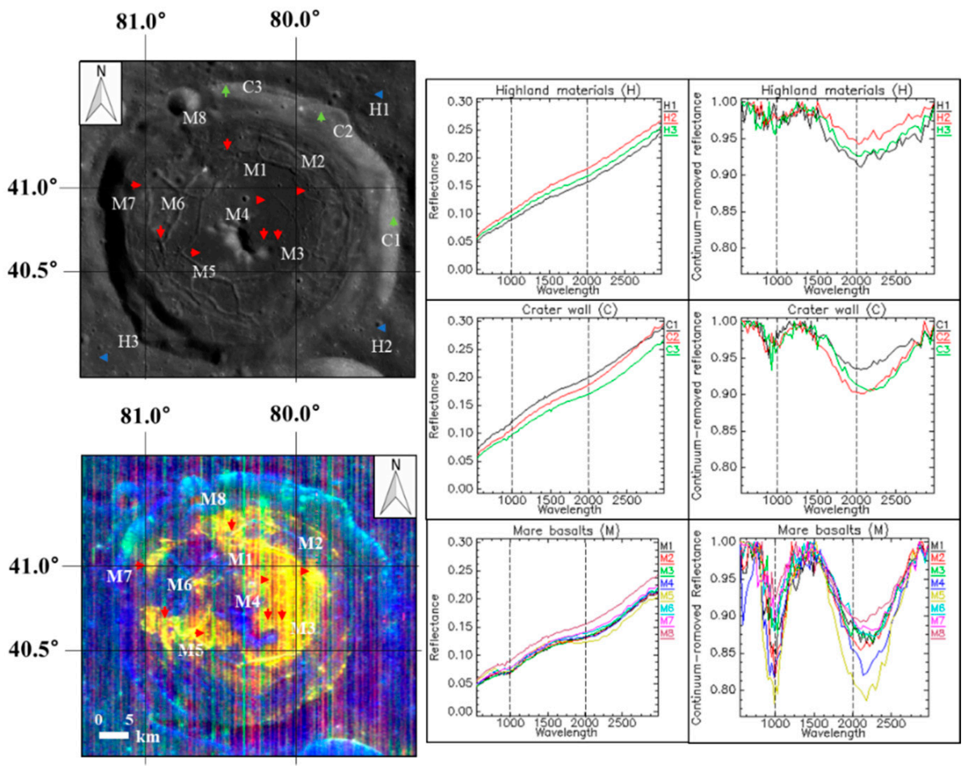

Figure 6. The WAC base map of the crater Lavoisier E (Figure 4b) shows the locations in the highlands (H1–H3), crater wall (C1–C3), and mare basalts (M1–M8). The WAC base map was taken from https://quickmap.lroc.asu.edu, accessed on 1 April 2022. To the right, the corresponding reflectance spectra and continuum-removed spectra are shown. The dashed lines in the spectra indicate the wavelengths of 1000 nm and 2000 nm. On the lower left, the RGB composite derived from the M^3 level 2 data is shown.

In Figure 5, the craters Lavoisier and Lavoisier F show various absorption bands in the reflectance spectra and continuum-removed spectra. The M7 spectrum in the mare basalts (M1–M7) in Figure 5 (pink-color spectrum) has absorption features similar to the high-Ca pyroxene, i.e., near 1000 nm and 2100 nm. Characteristic mare basalts are located near the floor-fractured regions in the crater. The 10 spectra cF1–cF11, except for cF4, clearly show absorption features such as low-Ca pyroxene, i.e., at below 1000 nm and near 2000 nm. Most of the sampled points (cF2, cF3, cF5, and cF7–cF10) are located near impact craters. However, cF4 is located in the floor-fractured region, and the spectrum shows absorption features similar to high-Ca pyroxene.

The crater Lavoisier E (Figure 6) shows reflectance spectra and continuum-removed spectra of the highland materials, crater wall, and mare basalts. Although the spectra of the highlands cannot be distinguished based on pronounced absorption features, the spectra of the crater wall are clearly similar to those of highland materials. The absorption features of the mare basalts occur near 1000 nm and near 2100 nm [32] because of small amounts of olivine or high-Ca pyroxene [58–60]. Among the mare basalts, locations M2 and M4 display the most distinct absorption features because they are located near fresh, small impact craters. The spectra of locations M6, M7, and M8 located near the floor-fractured regions do not reveal clear absorption features.

The crater Lavoisier H (Figure 7) shows the reflectance and continuum-removed spectra of the highland materials, crater wall, and dark mantle deposits. The spectra of the highland materials and the crater wall are similar to the highland and crater wall spectra in Figure 6 (Lavoisier E). The continuum-removed spectra of the mare basalts around the floor-fractured regions have faint absorption features below 1000 nm and beyond 2000 nm, which is typical of high-Ca pyroxene. The spectra of D2, D5, D7, and D8 located in the dark mantle deposits display relatively clear absorption features typical of low-Ca pyroxene because D2, D5, and D7 are situated near small impact craters with immature ejecta. However, D8 is located near a bright floor-fractured region, which appears to consist of Mg-rich rocks showing a distinct absorption feature near 2000 nm (green in Figure 4).

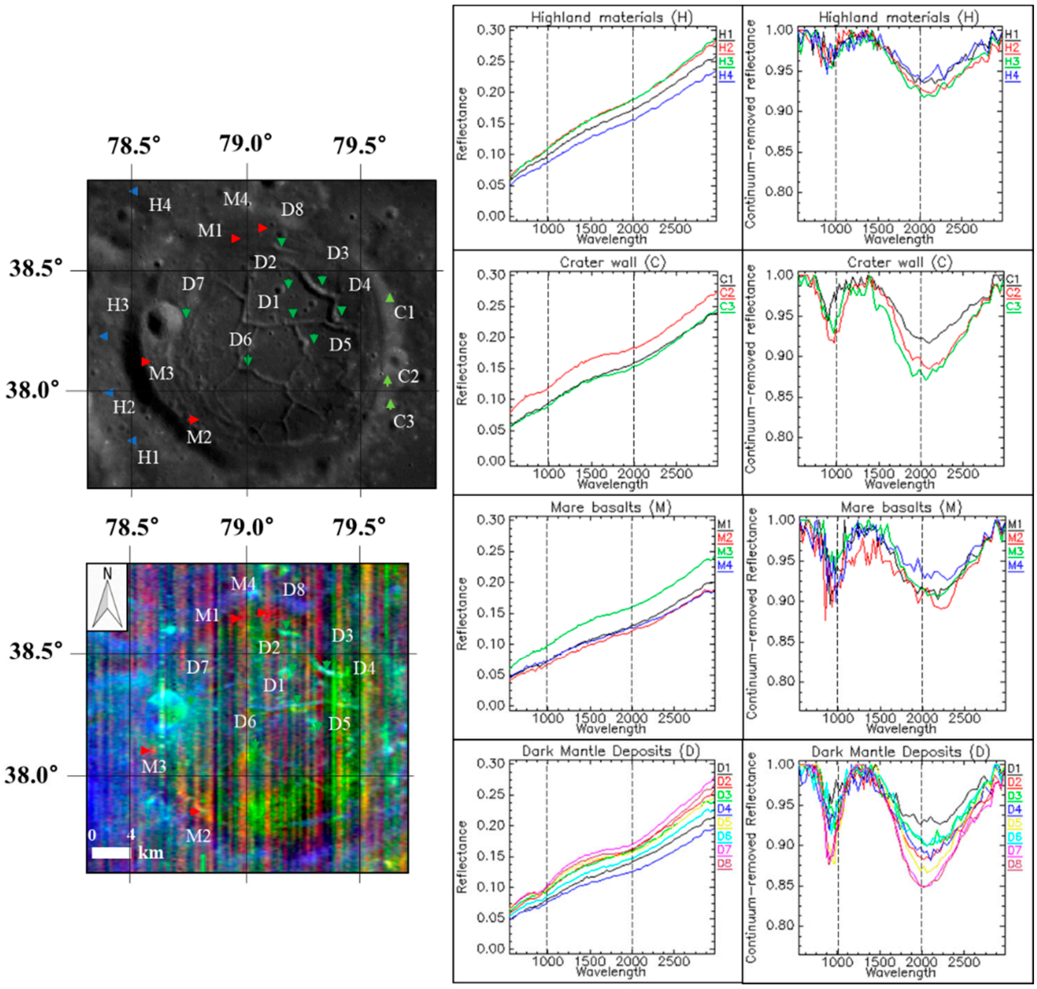

Figure 7. The WAC base map (Figure 4c) shows the locations in the highlands (H1–H4), crater wall (C1–C3), mare basalts (M1–M4), and dark mantle deposits (D1–D8). The WAC base map was taken from https://quickmap.lroc.asu.edu, accessed on 1 April 2022. To the right, the corresponding reflectance spectra and continuum-removed spectra are shown. The dashed lines in the spectra indicate the wavelengths of 1000 nm and 2000 nm. On the lower left, the RGB composite derived from the M^3 level 2 data is shown.

Figure 8 shows the reflectance and continuum-removed spectra of the crater wall of and mare basalts inside the crater Lavoisier C. The continuum-removed spectra of the crater wall have a pattern similar to those of C2 and C3 in the Lavoisier H Crater wall (Figure 7). The spectra of the mare basalts have absorption features near 1000 nm and 2100 nm typical of high-Ca pyroxene, like the mare basalts on the Lavoisier E Crater floor. The spectra of locations M1 and M2 are similar to the spectra of M3–M8 inside the crater. The spectra of M4 and M5 have relatively clear and pronounced absorption features because of their location near small and fresh impact craters with immature ejecta, such as those associated with locations M2 and M4 in the crater Lavoisier E (Figure 6).

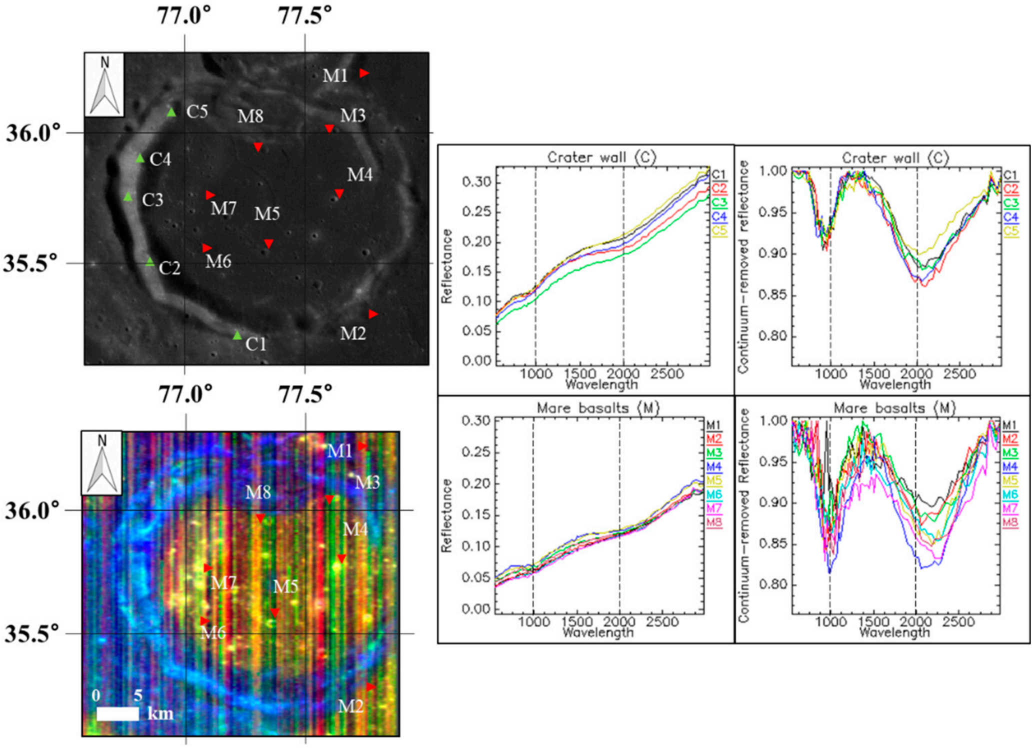

Figure 8. The WAC base map of the crater Lavoisier C (Figure 4d) shows the locations in the crater wall (C1–C5) and mare basalts (M1–M8). The WAC base map was taken from https://quickmap.lroc.asu.edu, accessed on 1 April 2022. To the right, the corresponding reflectance spectra and continuum-removed spectra are shown. The dashed lines in the spectra indicate the wavelengths of 1000 nm and 2000 nm. On the lower left, the RGB composite derived from the M^3 level 2 data is shown.

3.3. Spectral Identification of Minerals

Figure 9 shows the band I (~1000 nm) and band II (~2000 nm) center plots. The absorption band centers are identified as two groups I and II. The case of the craters Lavoisier/Lavoisier F and Lavoisier H (group I, low-Ca pyroxene, orthopyroxene in the norite) reveals absorption band centers similar to those present in library spectra of pigeonite [19,52,60,61]. The absorption band centers of Lavoisier E and Lavoisier C are located in the upper right part of the diagram (group II, high-Ca pyroxene) where the band centers of subcalcic augite are shown as yellow-diamond symbols and open-circle symbols. A few band centers of spectra of the crater Lavoisier E are located near diopside (orange-colored square of Adams [52]).

In Figures 4–8, the spectra of the Lavoisier E Crater (Figure 6) might exhibit another spectral feature, i.e., an absorption features near 600 nm [62–64]. Further investigation is required for a conclusion about this absorption anomaly near 600 nm for the spectrum M4 in Lavoisier E. Considering a comparison of reference band centers of lunar samples with the reflectance features of our study area, it appears that Lavoisier and its satellite craters of high interest with respect to the presence of lunar resources for future lunar ISRU (in-situ resource utilization) of Fe-rich minerals.

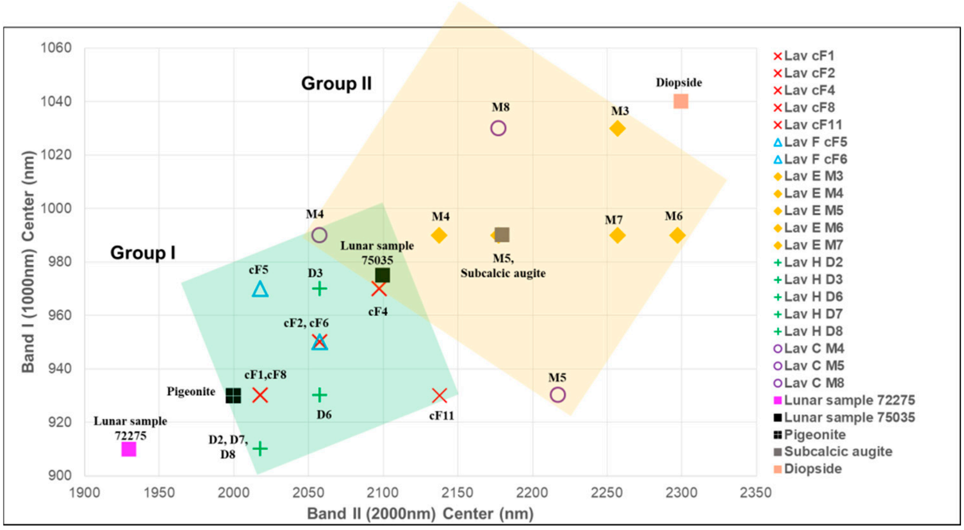

Figure 9. The reflectance features of the crater floor materials, mare basalts, and the dark mantle deposits (Figure 5 to Figure 8) on the five crater floors. They show the locations of band I (1000 nm) center and band II (2000 nm) center of the reflectance spectra. The colors for each point follow as: (crater floor, cF) cF1, cF2, cF4, cF8, and cF11 in the Lavoisier Crater (Lav)—red crosses, cF5 and cF6 in the Lavoisier F Crater (Lav F)—blue triangles (Figure 5), M3, M4, M5, M6, and M7 in the Lavoisier E Crater (Lav E)—orange diamonds (mare basalts, M) (Figure 6), D2, D3, D6, D7, and D8 in the Lavoisier H Crater (Lav H)—green crosses (dark mantle deposits, D) (Figure 7), M4, M5, and M8 in the crater Lavoisier C (Lav C)—purple circles (Figure 8), lunar sample 72275—pink square (orthopyroxene), lunar sample 75035—black square (subcalcic augite), pigeonite—black square, subcalcic augite—grey square, diopside—orange square. The five samples (diamonds and triangles) are adopted from Adams [52]. The overlapping points are as follows: Lavoisier (Lav) cF1, cF2, and cF8, Lavoisier F (Lav F) cF6, Lavoisier H (Lav H) D2, D7, and D8.

3.4. Morphological Investigation of Studied Region

Figure 10 shows the WAC base map (left column) of the study areas, the slopes (middle column), and aspects (the azimuth angle of the slopes) analysis (right column). The resolution of the topographic data used is 512 pixels/degree (SLDEM2015). The mare basalts areas of each crater are mostly flat except for the fractured regions. The dark mantle deposits are located near the floor-fractured regions.

The floor-fractured regions between the crater floors of Lavoisier and Lavoisier F have steep slopes similar to those in the crater wall. Those regions are included the cF4 region near the dark mantle deposits. The Lavoisier E Crater floor comprises relatively steep areas in the floor-fractured regions located in the northwest. The locations D1, D3, D4, and D6 on the floor of Lavoisier H are situated near the steep and floor-fractured regions. The crater floor of Lavoisier C shows a slope of 12° or less (white and pink) like the center of the floor of Lavoisier E, and the slopes of locations M3–M8 are similar to those found in Oceanus Procellarum (M1 and M2).

The aspect analysis (right image in Figure 10) of the five craters show the slope direction of the terrain. The southeast floor of Lavoisier, the northwestern floor of Lavoisier E (Lav E), and the floor of Lavoisier H (Lav H) appear complicated because of the floor-fractured regions, as already found in the slope analysis. The floor-fractured region near cF4 in the crater Lavoisier trends to the west (red). The fractures near D1, D3, D4, and D6 on the Lavoisier H Crater floor and M7 and M8 on the Lavoisier E Crater floor trends toward the south (blue).

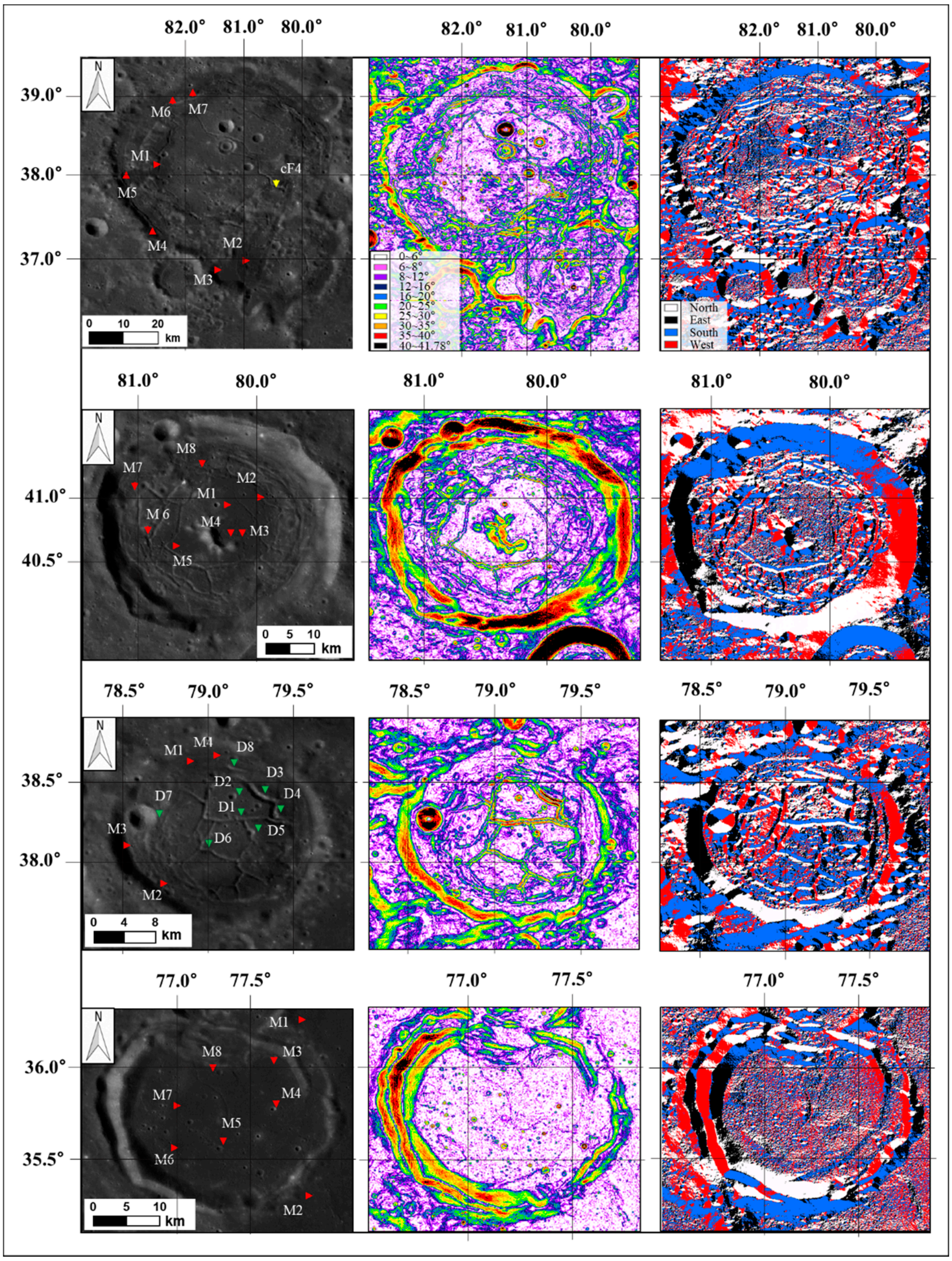

Figure 10. The WAC base map (**left**), the slope analysis (**middle**), and the aspect analysis (**right**) using the SLDEM2015 dataset of our study area. The points each for crater indicate the mare basalts, the dark mantle deposits, and the crater floor. The cF4 in the Lavoisier Crater is located near the dark mantle deposits. The colors in the slope analysis represent the range of slope degree: white (0~6°), pink (6~8°), purple (8~12°) navy (12~16°), blue (16~20°), green (20~25°), yellow (25~30°), orange (30~35°), red (35~40°), and black (40~71.48°). The right images show the direction of the slope in colors: white—north (315~360° and 0~45°), black—east (45~135°), blue—south (135~225°), and red—west (225~315°).

4. Discussion

The main usefulness of the Ca maps for our analysis is due to the fact that Mg-suite rocks, such as norite, and the main minerals in them, especially orthopyroxene, have a very low Ca content, much less than "typical", clinopyroxene-bearing mare basalt. The highest Ca content is observed for highland material dominated by plagioclase minerals, in particular anorthite ($CaAl_2Si_2O_8$), the Ca-rich endmember of the plagioclase series (Figure 3).

According to Thesniya and Rajesh (2020) [60], hyperspectral data from the Moon Mineralogy Mapper onboard the Chandrayaan-1 mission shows that the major minerals of the mare basalts are pigeonite ($(Ca,Mg,Fe)(Mg,Fe)Si_2O_6$)) and augite ($(Ca,Na)(Mg,Fe,Al,Ti)(Si,Al))_2O_6$). The Ca content in pigeonite is lower than in augite. According to Adams [52], the absorption features of pigeonite are located near 900 and 2000 nm in the spectra, whereas the absorption features of augite are centered near 1000 nm and 2100 nm. In the petrological and mineralogical analysis, the IBD2000 values in the composites of Figure 4 (indicating orthopyroxene ($(Mg,Fe,Ca)(Mg,Fe,Al)(Si,Al)_2O_6$) in noritic rock or low-calcium pyroxene (pigeonite)) shows the difference between mare basalts and dark mantle deposits. In Figure 5 to Figure 8, the spectra of the mare basalts and the dark mantle deposits also have absorption features similar to orthopyroxene with band centers being shifted toward shorter wavelengths by Ca (low-Ca pyroxene) and high-Ca pyroxene. In Figure 5 (Lavoisier and Lavoisier F) and Figure 7 (Lavoisier H), the spectra appear to show the absorption features of pigeonite. However, the spectra of Figure 6 (Lavoisier E) and Figure 8 (Lavoisier C) show absorption features that look like those of subcalcic augite.

Our finding of mixed materials (orthopyroxene with a band center shifted because of decreased Ca content) or low-calcium pyroxene (pigeonite, ferrosilite ($Fe_2Si_2O_6$), wollastonite ($CaSiO_3$), etc.) suggests the possibility that the materials ascended from the lower crust were connected to the crater floor from the fractured regions in the subsurface by the impact. That is, if the floors of the floor-fractured craters were uplifted because of shallow magmatic intrusion and sill formation [7–9,20], these materials would be expected to reach up to the crater floor. This mechanism supports the possibility that the materials were mixed with highland material by impacts [15] or that the materials are buried in the highland crust because of the ejecta of younger impact craters [13]. The basaltic lava and the relatively Mg-rich rocks (or minerals) represented by red and green colors, respectively, in the petrological maps are exposed along the cracked penetration path of the crater floor, as in the craters Lavoisier, Lavoisier F, Lavoisier E, and Lavoisier H [7]. According to Besse et al. [32], the mineral spectra show strong absorption bands at 1000 nm and near 2000 nm, or shifted absorption bands beyond 1000 nm and 2000 nm because of the presence of highland components (e.g., Appendix D: cF4 and cF11 on the Lavoisier Crater floor; D2, D7, and D8 in the crater Lavoisier H).

Another possibility is that the exposed materials are from a place near large maria (e.g., Oceanus Procellarum). The craters Lavoisier and Lavoisier F are located several tens of kilometers away from Oceanus Procellarum. The spectra of the crater floor in Figure 6 (Lavoisier E) and Figure 8 (Lavoisier C) have absorption features similar to Oceanus Procellarum (surrounding area in Figure 8). The mare basalts on the Lavoisier E Crater floor may thus have mineral characteristics similar to those of Oceanus Procellarum (Figure 1). One possible explanation is that the sills or dikes on the crater floor of Lavoisier E are connected with the western part of Oceanus Procellarum. In addition, the mare basalts on the Lavoisier E Crater floor may have mixed with melted materials after an impact [65]. Another possibility is that the parts of the lower crust materials beneath the crater floor did not reach the crater floor through fissures or floor-fractured terrains because of a weak impact on the lunar surface or because of a thick crust beneath the crater [66]. Sometimes floor-fractured craters are produced without the eruption of lava from the surface, only by intrusion of a sill into the shallow subsurface [7].

Through these possibilities, the mare basalts and the dark mantle deposits exposed at the lunar surface could be low-Ca pyroxene (LCP) or high-Ca pyroxene (HCP). The Mg-suite rocks, dark mantle deposits or mare basalts on the crater floor are particularly important clues because they mainly originate from the lower crust and upper mantle.

Therefore, we can assume the origin of the uplifted or exposed materials for each crater as follows. The crater Lavoisier E is similar to Lavoisier C in that parts of its floor are flooded by basaltic material. In particular, the edge of the crater Lavoisier C in Figure 4d makes it appear that part of the crater was buried by mare basalts. According to Taguchi [10], mare basalts flooding the area altered the surrounding terrain (craters, sill, etc.). Craters lower than the region surrounding the mare basalts were covered up to the crater floor or to parts of the crater wall.

The proposed sequence of geological events that led to the formation of the structures observed in the Lavoisier area is illustrated in Figure 11. The times of occurrence of the events is marked by T1, T2, T3 and T4, where T1 marks the earliest event and T4 marks the most recent event (T1 > T2 > T3 > T4). Letters mark events within each period that occurred at more or less the same time. We assume that the upper lunar mantle mainly provided basaltic magma (red), the lower crust noritic (Mg-suite [67]) material (green), and the upper crust feldspathic material rich in plagioclase (blue).

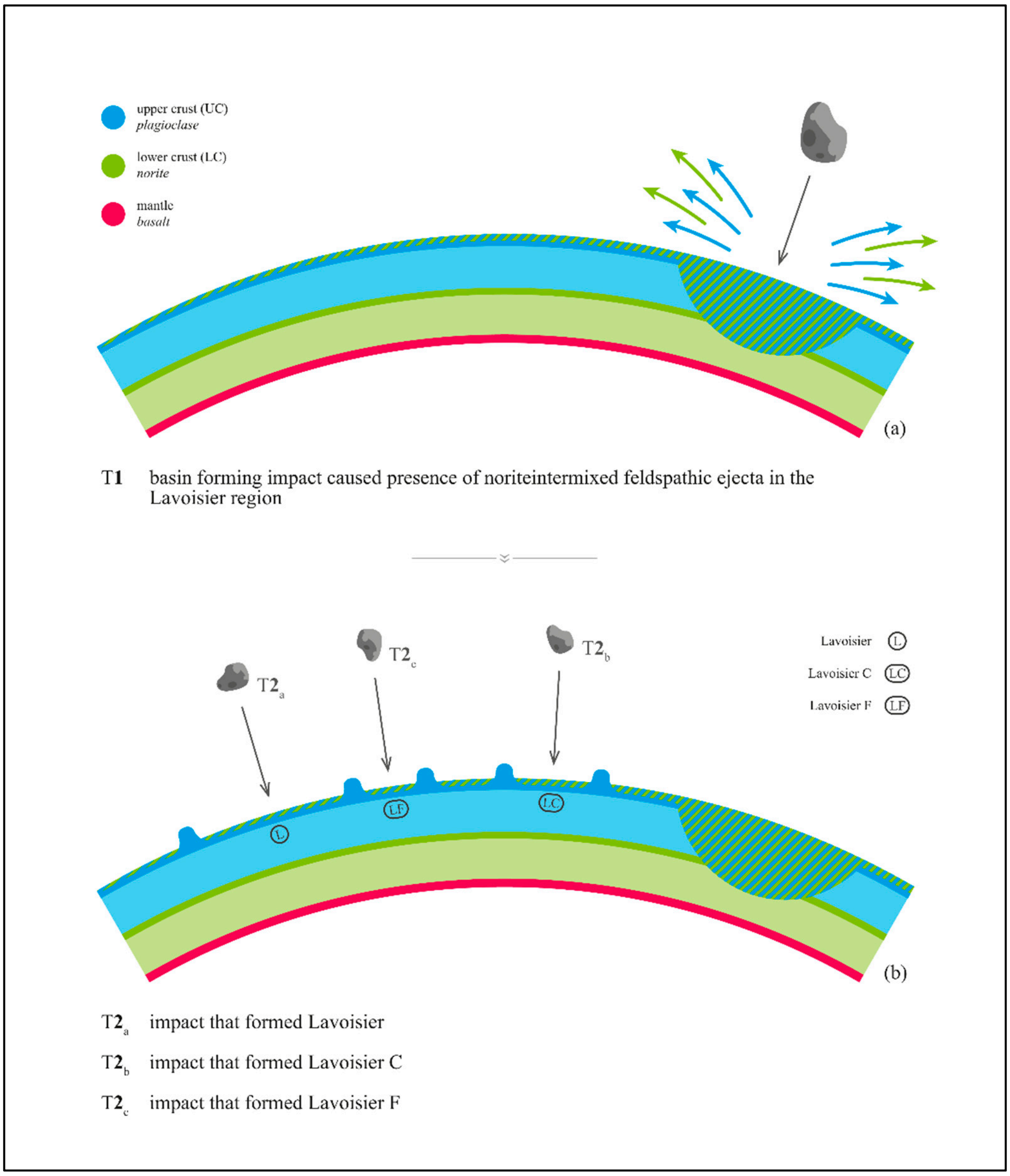

Figure 11. *Cont.*

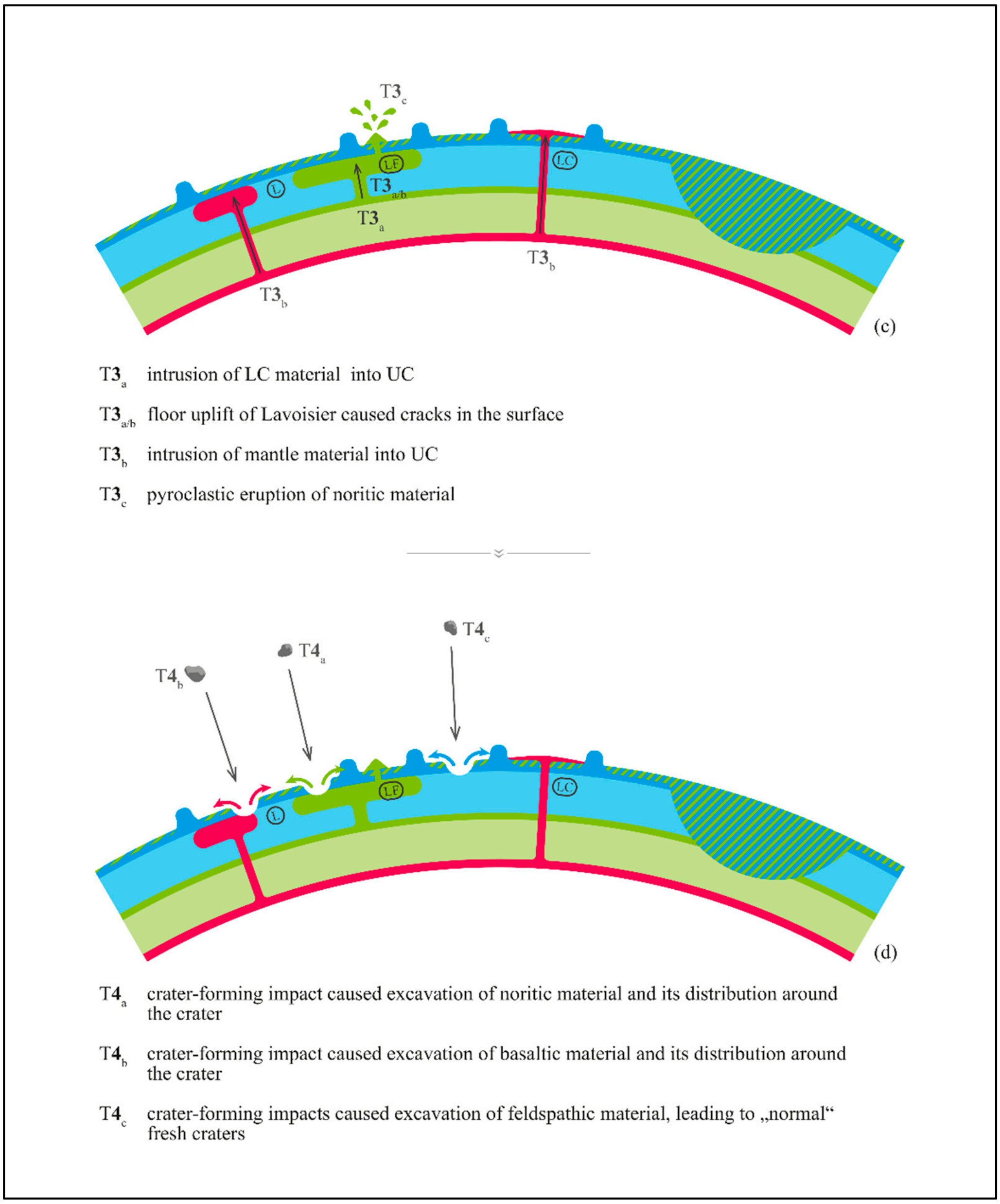

Figure 11. The schematic illustration of the proposed geologic processes that generated the morphological and petrological structures observed in the Lavoisier region. The times of occurrence of the events are denoted by T1 (first event) > T2 > T3 > T4 (most recent events). Letters mark events that occurred approximately simultaneously within each period and do not indicate a temporal sequence. (**a**) Period T1, formation of a nearby impact basin with norite-intermixed feldspathic ejecta. (**b**) Period T2, formation of Lavoisier and its large satellite craters. (**c**) Period T3, magmatic intrusion and flooding processes and pyroclastic eruption. (**d**) Period T4, formation of small impact craters ejecting basaltic, noritic or feldspathic material. For details, see Sections 1–4.

The first event is the formation of one or several nearby large impact basins at time T1. This impact excavated noritic material from the lower crust together with feldspathic material from the upper crust, thus distributing norite-intermixed feldspathic ejecta across a large area near the border of Oceanus Procellarum, which appear in blue-green in our petrologic maps (see also Figure 12). Notably, the Mg-rich materials surrounding the major nearside mare areas were detected independently by Berezhnoy et al. [27] based on Lunar Prospector Gamma Ray Spectrometer data.

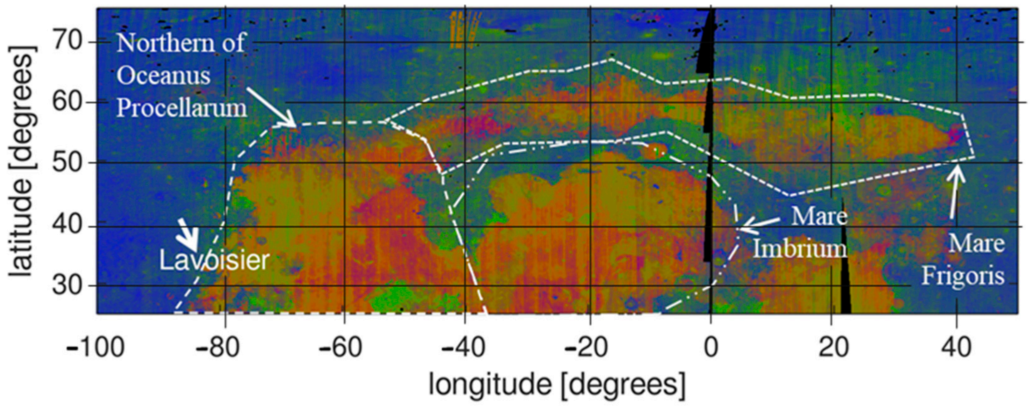

Figure 12. Petrological map of Mare Frigoris, northern Oceanus Procellarum, and northern Mare Imbrium. Mare basalt areas appear in red/orange color. The northern Imbrium Noritic anomaly [68] corresponds to the green area surrounding Mare Frigoris. This noritic area extends to the west until the northern and northwestern rims of Oceanus Procellarum and transitions into the Lavoisier region.

The impact basin formed at time T1 may be one of the multitudes of lava-covered impact basins in the Oceanus Procellarum area [69] or the South Pole–Aitken basin. In the latter case, the Lavoisier area would have to be considered as a western extension of the northern Imbrium Noritic anomaly, with the noritic material corresponding to antipodal ejecta of the South Pole–Aitken basin [68]. The impacts during the period T2 formed the large craters Lavoisier, Lavoisier C and F, and also Lavoisier E and H (events at times T2a, T2b and T2c). The formation of these craters was followed by the intrusion of noritic lower crust material (T3a) and basaltic upper mantle material (T3b) into the upper crust below the large craters. These intrusions led to the floor uplift (T3a/b) and fracture formation in the crater floors still visible today as linear rilles or cracks. The small concentric crater on the floor of Lavoisier may also be a result of these magmatic intrusions [70,71]. Furthermore, basaltic material ascended either from an intrusive basaltic magmatic body or directly from the upper mantle to the surface and flooded the floor of Lavoisier C (T3b). The pyroclastic eruption of a probably small fraction of the intruded noritic material emplaced the large and distinct dark mantle deposits on the floor of Lavoisier F (T3c), which appears as Mg-suite material in our petrologic map. On the floor of the crater Lavoisier, more recent impacts penetrated through the norite-intermixed feldspathic upper crustal layer, formed small craters and distributed noritic material (T4a, northern part of Lavoisier floor) and basaltic material (T4b, near the northern inner wall of Lavoisier) around them. Outside the uplift area, a multitude of small craters was formed by similar small impacts, which distributed feldspathic material of the upper crust around them (T4c). This proposed sequence of events is able to explain the morphological and petrological structures observed in the Lavoisier region.

Given the sequence of geological events of Figure 11, it is interesting to estimate the excavation depths of the impacts to infer the likely origin of the excavated and distributed materials. We cannot assign the basin-forming impact at time T1 to a specific basin in the nearby Oceanus Procellarum area, though, so we cannot determine the depth of origin of the widespread Mg-suite material intermixed with feldspathic crustal material and apparent all over the Lavoisier area. In contrast, the excavation depths of the crater-forming impacts indicated in Figure 11 can be obtained using basic scaling laws. As pointed out by Liu et al. [72], it is commonly assumed that for simple lunar craters ($D < 21$ km) the excavation depth corresponds to $D_e\ [\mathrm{km}] = 0.08\ D\ [\mathrm{km}]$ and for complex lunar craters ($D > 21$ km) to $D_e\ [\mathrm{km}] = 0.1 \times \left(D\ [\mathrm{km}] \times 21^{0.13}/1.17\right)^{1/1.13}$. The diameters of the craters Lavoisier, Lavoisier C, and Lavoisier F (Figure 11b) correspond to 68 km, 30 km, and 32 km, respectively, such that they excavated material from depths of 5.2 km, 2.5 km, and 2.7 km. Hence, these impacts probably did not penetrate the upper lunar crust. The small impact craters indicated in Figure 11d have diameters of 4.8 km (T4a), 1.1 km (T4b), and 3.6 km

(T4c), leading to excavation depths of about 400 m, 900 m, and 300 m. This suggests that intrusion processes occurring at time T3 transported the basaltic and Mg-suite materials to shallow depths below the surface. Furthermore, the excavation depth of the T4c crater hints at an intermixed feldspathic–Mg-suite surface layer of at most a few hundred meters thickness, underlain by relatively pure feldspathic material.

5. Conclusions

The petrological, mineralogical, and morphological methods used in this study offer an effective approach that can distinguish the relatively flat mare basalts regions, the rough crater floor, and floor-fractured regions. This study demonstrates that false color (RGB) composite analyses using petrological and mineralogical investigations of lunar craters are essential for upcoming studies involved in lunar geology and in situ resource utilization.

We confirm the existence of mare basalts and dark mantle deposits, which were then used to identify minerals exposed on the crater surfaces of Lavoisier and surrounding craters using reflectance spectra. The mare basalts on parts of the crater floors of Lavoisier C and E show shifted absorption features near 1000 nm and 2100 or 2200 nm, e.g., the absorption feature of high-Ca pyroxene. This may be due to mixing with Imbrium ejecta components as indicated by Nakamura et al. [15]. These features confirm that these craters have impact-associated features (as indicated in the USGS Digital Unified Global Geologic Map of the Moon [30]). Two mineral groups (I and II in Figure 9) of subcalcic augite and pigeonite (or orthopyroxene in the norite) were identified in the study area.

The reason why mare basalts exist in Lavoisier C and E may be due to underground passages (e.g., sills or dikes) that could be exposed source materials for basaltic lava beneath the impact crater (Figure 11). We also confirmed the mare basalts and the dark mantle deposits in the floor-fractured regions of Lavoisier, Lavoisier E, F, and H were also found on steep terrain on the crater floor through morphological analysis. Furthermore, we developed a model of the temporal sequence of events that is able to explain the morphologic, spectral, and petrologic properties of the Lavoisier region and the geologic structures observed in it.

So far, our study has been focused on the process of uplifting and exposing the crater floor because of shallow magmatic intrusion in the fractured regions. An additional investigation of regions between Oceanus Procellarum and the highlands is needed to apply the techniques used in this study (e.g., the western and southwestern regions between Oceanus Procellarum and the highlands). In particular, the regions between Oceanus Procellarum and the Orientale Basin have many craters with mare basalts. Further investigation of the above regions might be targeted to investigate both lunar geological evolution and resources.

Author Contributions: Data curation, E.S.Y.; Formal analysis, E.S.Y., C.W. and A.A.B.; Funding acquisition, K.J.K.; Investigation, E.S.Y., K.J.K., C.W., A.A.B., Y.H.K. and S.M.; Methodology, E.S.Y. and C.W.; Supervision, K.J.K. and Y.H.K.; Validation, C.W. and A.A.B.; Writing—review & editing, A.A.B. and C.W. All authors have read and agreed to the published version of the manuscript.

Funding: This research was funded by the Ministry of Science, ICT and Future Planning (MSIP), grant number 2016M1A3A9913307 (KIGAM 22-6801).

Data Availability Statement: The petrological and elemental abundance data generated in this study based on M^3 level1B spectral radiance data are available on request from the corresponding author.

Acknowledgments: Data were downloaded from the NASA Planetary Data System (PDS) Geoscience Node Lunar Orbital Data Explorer (ODE) (https://ode.rsl.wustl.edu/moon/, accessed on 26 November 2021) and NASA's Planetary Geology, Geophysics and Geochemistry Laboratory (PGDA) (https://pgda.gsfc.nasa.gov/products/54, accessed on 16 March 2021). A.A.B. was supported by Russian Science Foundation grant no. 20-12-00105 and by the Kazan Federal University Strategic Academic Leadership Program ("Priority-2030"). The authors are grateful to Marcel Hess for his help with the data analysis software. Furthermore, the authors wish to thank Alexander Wöhler for laying out the geological sketch of Figure 11.

Conflicts of Interest: The authors declare no conflict of interest.

Appendix A

Table A1. The floor-fractured craters (FFCs) in the study area that include the dark mantle deposits and mare basalts list in Figure 1 (IAU Gazetteer of Planetary Nomenclature_Moon).

	Name	Diameter [km]	Center Latitude/Longitude [Degrees]	Image Used (Lunar Orbital Data Explorer, M3 Data)
FFCs, dark mantle deposits, and mare basalts	Lavoisier	71.01	38.00°N/80.10°W	M3g20090712t053922_v01_rfl & M3g20090614t135122_v01_rfl
	Lavoisier C	34.9	35.77°N/76.78°W	M3g20090614t135122_v01_rfl
	Lavoisier E	40.88	40.87°N/80.45°W	M3g20090614t175501_v01_rfl
	Lavoisier F	37.03	36.40°N/76.40°W	
	Lavoisier H	38.17	38.15°N/78.90°W	

Appendix B

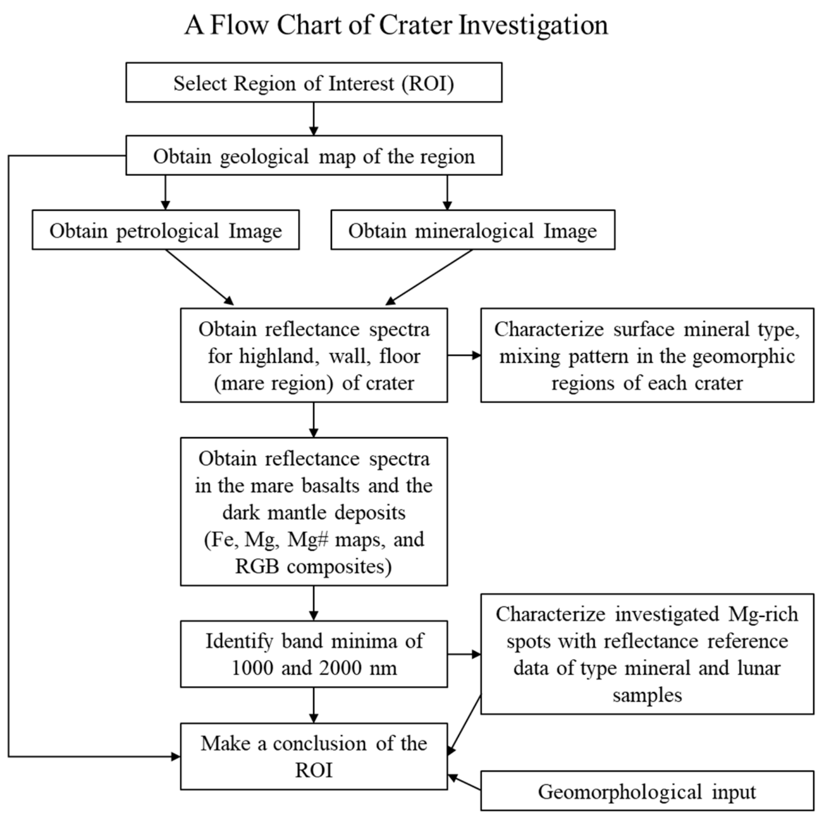

Figure A1. A flow chart of crater investigation described in this study.

Appendix C

Table A2. The location for each spectrum from Figure 5 to Figure 8 (the data were downloaded from https://quickmap.lroc.asu.edu, accessed on 8 January 2020, updated on 20 May 2020).

	Name	Region for Each Spectrum		Latitude/Longitude [Degrees]
Study area	Lavoisier and Lavoisier F	Highland materials	H1	36.3067°N/82.6820°W
			H2	37.0094°N/82.7743°W
			H3	38.9682°N/82.9289°W

Table A2. *Cont.*

	Name	Region for Each Spectrum		Latitude/Longitude [Degrees]
Study area	Lavoisier and Lavoisier F	Mare basalts	M1	38.1299°N/82.0146°W
			M2	36.9125°N/81.3164°W
			M3	36.9015°N/81.30512°W
			M4	38.0384°N/82.5047°W
			M5	39.0097°N/81.6745°W
			M6	38.9454°N/81.9143°W
			M7	39.0111°N/81.6631°W
		Crater Floor	cF1	38.6637°N/81.1817°W
			cF2	38.6041°N/81.0351°W
			cF3	38.5228°N/80.8295°W
			cF4	37.8880°N/80.6369°W
			cF5	37.1337°N/80.5528°W
			cF6	36.8896°N/80.4605°W
			cF7	38.0238°N/80.9476°W
			cF8	38.2273°N/81.2216°W
			cF9	38.3846°N/81.4631°W
			cF10	38.2408°N/81.6856°W
			cF11	37.8284°N/81.6612°W
	Lavoisier E	Highland materials	H1	41.6304°N/79.4765°W
			H2	40.3471°N/79.4602°W
			H3	40.1843°N/81.4272°W
		Crater wall	C1	40.9684°N/79.3436°W
			C2	41.5571°N/79.8536°W
			C3	41.7049°N/80.5287°W
		Mare basalts	M1	41.0552°N/80.2470°W
			M2	41.1095°N/79.9622°W
			M3	40.8397°N/80.1726°W
			M4	40.8352°N/80.2620°W
			M5	40.7622°N/80.7083°W
			M6	40.8464°N/80.9971°W
			M7	41.1749°N/81.1021°W
			M8	41.3425°N/80.5256°W
	Lavoisier H	Highland materials	H1	37.8240°N/79.5333°W
			H2	37.9852°N/79.6296°W
			H3	38.1810°N/79.6552°W
			H4	38.6825°N/79.5182°W
		Crater wall	C1	38.3365°N/78.3691°W
			C2	38.0533°N/78.3796°W
			C3	37.9690°N/78.3736°W

Table A2. *Cont.*

	Name	Region for Each Spectrum		Latitude/Longitude [Degrees]
Study area	Lavoisier H	Mare Basalts	M1	38.5289°N/79.0302°W
			M2	37.8903°N/79.1944°W
			M3	38.0981°N/79.3977°W
			M4	38.55877°N/78. 9105°W
		Dark mantle deposits	D1	38.2462°N/78.7930°W
			D2	38.3502°N/78.8171°W
			D3	38.3577°N/78.6680°W
			D4	38.2598°N/78.5837°W
			D5	38.1664°N/78.7087°W
			D6	38.0414°N/79.0024°W
			D7	38.2462°N/79.2704°W
			D8	38.5008°N/78.8457°W
	Lavoisier C	Crater wall	C1	35.2459°N/76.8265°W
			C2	35.5423°N/77.2355°W
			C3	35.8134°N/77.3369°W
			C4	35.9703°N/77.2830°W
			C5	36.1606°N/77.1356°W
		Mare Basalts	M1	36.3003°N/76.2107°W
			M2	35.3137°N/76.1647°W
			M3	35.9656°N/76.2796°W
			M4	35.7183°N/76.2811°W
			M5	35.4900°N/76.5998°W
			M6	35.5788°N/76.9549°W
			M7	35.7991°N/76.9295°W
			M8	35.9164°N/76.5982°W

Appendix D

Table A3. The detected minerals of the points for each crater in Figure 9.

	Geologic Units * in Figure 1	Clinopyroxene		Orthopyroxene (Shifted by Ca) in the Norite
		Subcalcic Augite	Pigeonite	
Lavoisier	pNc, Nc, Ip	cF4, cF11	cF1, cF2, cF4, cF8, cF11	cF1, cF8
Lavoisier F	pNc, Nc, Ip	cF5, cF6	cF5, cF6	
Lavoisier E	NC, Im2	M3, M4, M5, M6, M7, M8 (Figure 6)		
Lavoisier H	pNc	D3	D2, D3, D6, D7, D8, D1 (Figure 7), D4 (Figure 7)	D2, D7, D8
Lavoisier C	Nc, Im2	M4, M5, M8		

* pNc, pre-Nectarian: −4.5 to −3.9 Ga; Nc, Nectarian: −3.9 to −3.8 Ga; Ip, Imbrian: −3.8 to −3.2 Ga.

Table A4. The minimum point values (abbreviations for each terrain *) for each crater in Figure 9.

Region/Minimum Points	Absorption Feature (nm) (Near 1000)	Absorption Feature (Band Point) (Value)	Absorption Feature (nm) (Near 2000)	Absorption Feature (Band Point) (Value)
Lav cF1	930.1	0.879	2018.0	0.793
Lav cF2	950.0	0.917	2057.9	0.873
Lav cF4	970.0	0.927	2097.8	0.885
Lav cF8	930.1	0.880	2018.0	0.843
Lav cF11	930.1	0.908	2137.8	0.876
Lav F cF5	970.0	0.916	2018.0	0.887
Lav F cF6	950.0	0.820	2057.9	0.775
Lav E M3	1029.9	0.877	2257.5	0.865
Lav E M4	989.9	0.817	2137.8	0.820
Lav E M5	989.9	0.782	2177.7	0.786
Lav E M6	989.9	0.880	2297.4	0.873
Lav E M7	989.9	0.892	2257.5	0.881
Lav H D2	910.1	0.922	2018.0	0.882
Lav H D3	970.0	0.913	2057.9	0.900
Lav H D6	930.1	0.914	2057.9	0.899
Lav H D7	910.1	0.882	2018.0	0.849
Lav H D8	910.1	0.876	2018.0	0.848
Lav C M4	989.9	0.814	2057.9	0.819
Lav C M5	930.1	0.842	2217.6	0.850
Lav C M8	1029.9	0.837	2177.7	0.847

* H (highland material), C (crater wall), cF (crater floor), M (mare basalts), and D (dark mantle deposits).

References

1. Wichman, R.W.; Schultz, P.H. Floor-fractured impact craters on Venus: Implications for igneous crater modification and local magmatism. *J. Geophys. Res. Earth Surf.* **1995**, *100*, 3233–3244. [CrossRef]
2. Schultz, P.H.; Orphal, D.L. Floor-fractured craters on the Moon and Mars. *Meteoritics* **1978**, *13*, 622–625.
3. Buczkowski, D.; Williams, D.; Scully, J.; Mest, S.; Crown, D.; Schenk, P.; Jaumann, R.; Roatsch, T.; Preusker, F.; Nathues, A.; et al. The geology of the occator quadrangle of dwarf planet Ceres: Floor-fractured craters and other geomorphic evidence of cryomagmatism. *Icarus* **2018**, *316*, 128–139. [CrossRef]
4. Schultz, P.H. Floor-fractured lunar craters. *Earth Moon Planets* **1976**, *15*, 241–273. [CrossRef]
5. Masursky, H. A Preliminary Report on the Role of Isostatic Rebound in the Geologic Development of the Lunar Crater Ptolemaeus. In *Astrogeologic Studies*; United States Geological Survey: Reston, VA, USA, 1964; pp. 102–134.
6. Daneš, Z.F. Rebound Processes in Large Craters. In *Astrogeologic Studies*; United States Geological Survey: Reston, VA, USA, 1965; pp. 81–100.
7. Jozwiak, L.M.; Head, J.W.; Zuber, M.T.; Smith, D.E.; Neumann, G. Lunar floor-fractured craters: Classification, distribution, origin and implications for magmatism and shallow crustal structure. *J. Geophys. Res. Earth Surf.* **2012**, *117*, E11005. [CrossRef]
8. Jozwiak, L.M.; Head, J.W.; Wilson, L. Lunar floor-fractured craters as magmatic intrusions: Geometry, modes of emplacement, associated tectonic and volcanic features, and implications for gravity anomalies. *Icarus* **2015**, *248*, 424–447. [CrossRef]
9. Wilson, L.; Head, J.W. Lunar floor-fractured craters: Modes of dike and sill emplacement and implications of gas production and intrusion cooling on surface morphology and structure. *Icarus* **2018**, *305*, 105–122. [CrossRef]
10. Taguchi, M.; Morota, T.; Kato, S. Lateral heterogeneity of lunar volcanic activity according to volumes of mare basalts in the farside basins. *J. Geophys. Res. Planets* **2017**, *122*, 1505–1521. [CrossRef]
11. Snyder, G.A.; Taylor, L.A.; Neal, C.R. A chemical model for generating the sources of mare basalts: Combined equilibrium and fractional crystallization of the lunar magmasphere. *Geochim. Cosmochim. Acta* **1992**, *56*, 3809–3823. [CrossRef]
12. Elkins-Tanton, L.T.; Burgess, S.; Yin, Q.-Z. The lunar magma ocean: Reconciling the solidification process with lunar petrology and geochronology. *Earth Planet. Sci. Lett.* **2011**, *304*, 326–336. [CrossRef]

13. Elardo, S.M.; Draper, D.S.; Shearer, C.K., Jr. Lunar Magma Ocean crystallization revisited: Bulk composition, early cumulate mineralogy, and the source regions of the highlands Mg-suite. *Geochim. Cosmochim. Acta* **2011**, *75*, 3024–3045. [CrossRef]
14. Moriarty, D.P.; Dygert, N.; Valencia, S.N.; Watkins, R.N.; Petro, N.E. The search for lunar mantle rocks exposed on the surface of the Moon. *Nat. Commun.* **2021**, *12*, 4659. [CrossRef] [PubMed]
15. Nakamura, R.; Yamamoto, S.; Matsunaga, T.; Ishihara, Y.; Morota, T.; Hiroi, T.; Takeda, H.; Ogawa, Y.; Yokota, Y.; Hirata, N.; et al. Compositional evidence for an impact origin of the Moon's Procellarum basin. *Nat. Geosci.* **2012**, *5*, 775–778. [CrossRef]
16. Gaddis, L.R.; Hawke, B.R.; Robinson, M.S.; Coombs, C. Compositional analyses of small lunar pyroclastic deposits using Clementine multispectral data. *J. Geophys. Res. Earth Surf.* **2000**, *105*, 4245–4262. [CrossRef]
17. Gaddis, L.R.; Staid, M.I.; Tyburczy, J.A.; Hawke, B.; Petro, N.E. Compositional analyses of lunar pyroclastic deposits. *Icarus* **2003**, *161*, 262–280. [CrossRef]
18. Gustafson, J.O.; Bell, J.F.; Gaddis, L.R.; Hawke, B.R.; Giguere, T.A. Characterization of previously unidentified lunar pyroclastic deposits using Lunar Reconnaissance Orbiter Camera data. *J. Geophys. Res. Earth Surf.* **2012**, *117*, E00H25. [CrossRef]
19. Sivakumar, V.; Neelakantan, R.; Santosh, M. Lunar surface mineralogy using hyperspectral data: Implications for primordial crust in the Earth–Moon system. *Geosci. Front.* **2017**, *8*, 457–465. [CrossRef]
20. Thorey, C.; Michaut, C. A model for the dynamics of crater-centered intrusion: Application to lunar floor-fractured craters. *J. Geophys. Res. Planets* **2014**, *119*, 286–312. [CrossRef]
21. Johnson, T.; Morrissey, L.; Nemchin, A.; Gardiner, N.; Snape, J. The phases of the Moon: Modelling crystallisation of the lunar magma ocean through equilibrium thermodynamics. *Earth Planet. Sci. Lett.* **2020**, *556*, 116721. [CrossRef]
22. Rencz, A.N.; Ryerson, R.A. (Eds.) *Manual of Remote Sensing*, *Remote Sensing for the Earth Sciences*; John Wiley & Sons: Hoboken, NJ, USA, 1999; Volume 3.
23. Stuart, B.H. *Infrared Spectroscopy: Fundamentals and Applications*; John Wiley and Sons Ltd.: Chichester, UK, 2004; ISBN 0470854278.
24. Heiken, G.H.; Vaniman, D.T.; French, B.M. Lunar Rocks. In *Lunar Sourcebook-A User's Guide to the Moon*; Cambridge University Press: Cambridge, UK, 1991; Chapter 6; pp. 183–284.
25. Morimoto, N.; Fabries, J.; Ferguson, A. Nomenclature of pyroxenes. *Mineral. J.* **1989**, *14*, 198–221. [CrossRef]
26. Wieczorek, M.A.; Jolliff, B.L.; Khan, A.; Pritchard, M.E.; Weiss, B.P.; Williams, J.G.; Hood, L.L.; Righter, K.; Neal, C.R.; Bussey, B.; et al. The constitution and structure of the lunar interior. *Rev. Mineral. Geochem.* **2006**, *60*, 221–364.
27. Berezhnoy, A.; Hasebe, N.; Kobayashi, M.; Michael, G.; Okudaira, O.; Yamashita, N. A three end-member model for petrologic analysis of lunar prospector gamma-ray spectrometer data. *Planet. Space Sci.* **2005**, *53*, 1097–1108. [CrossRef]
28. Wöhler, C.; Grumpe, A.; Berezhnoy, A.; Bhatt, M.U.; Mall, U. Integrated topographic, photometric and spectral analysis of the lunar surface: Application to impact melt flows and ponds. *Icarus* **2014**, *235*, 86–122. [CrossRef]
29. Bhatt, M.; Wöhler, C.; Dhingra, D.; Thangjam, G.; Rommel, D.; Mall, U.; Bhardwaj, A.; Grumpe, A. Compositional studies of Mare Moscoviense: New perspectives from Chandrayaan-1 VIS-NIR data. *Icarus* **2018**, *303*, 149–165. [CrossRef]
30. Fortezzo, C.M.; Spudis, P.D.; Harrel, S.L. Release of the digital unified global geologic map of the Moon at 1:5,000,000-Scale. In Proceedings of the Lunar and Planetary Science Conference, No. 2326, The Woodlands, TX, USA, 16–20 March 2020.
31. Wilhelms, D.E.; McCauley, J.F.; Trask, N.J. *The Geologic History of the Moon*; USGS Professional Paper 1348: For Sale by the Books and Open-File Reports Section; US Geological Survey: Menlo Park, CA, USA, 1987.
32. Besse, S.; Sunshine, J.M.; Gaddis, L.R. Volcanic glass signatures in spectroscopic survey of newly proposed lunar pyroclastic deposits. *J. Geophys. Res. Planets* **2014**, *119*, 355–372. [CrossRef]
33. Kumaresan, P.; Saravanavel, J.; Palanivel, K. Lithological mapping of Eratosthenes crater region using Moon Mineralogy Mapper of Chandrayaan-1. *Planet. Space Sci.* **2020**, *182*, 104817. [CrossRef]
34. Wöhler, C.; Grumpe, A.; Berezhnoy, A.A.; Feoktistova, E.; Evdokimova, N.A.; Kapoor, K.; Shevchenko, V.V. Temperature regime and water/hydroxyl behavior in the crater Boguslawsky on the Moon. *Icarus* **2017**, *285*, 118–136. [CrossRef]
35. Wöhler, C.; Grumpe, A.; Berezhnoy, A.A.; Shevchenko, V.V. Time-of-day–dependent global distribution of lunar surficial water/hydroxyl. *Sci. Adv.* **2017**, *3*, e1701286. [CrossRef]
36. Bhatt, M.; Wöhler, C.; Grumpe, A.; Hasebe, N.; Naito, M. Global mapping of lunar refractory elements: Multivariate regression vs. machine learning. *Astron. Astrophys.* **2019**, *627*, A155. [CrossRef]
37. Pieters, C.M.; Boardman, J.; Buratti, B.; Chatterjee, A.; Clark, R.; Glavich, T.; Green, R.; Head, J.; Isaacson, P.; White, M.; et al. The Moon Mineralogy Mapper (M^3) on Chandrayaan-1. *Curr. Sci.* **2009**, *96*, 500–505.
38. Bhatt, M.; Mall, U.; Wöhler, C.; Grumpe, A.; Bugiolacchi, R. A comparative study of iron abundance estimation methods: Application to the western nearside of the Moon. *Icarus* **2015**, *248*, 72–88. [CrossRef]
39. Lawrence, D.J.; Feldman, W.C.; Barraclough, B.L.; Binder, A.B.; Elphic, R.C.; Maurice, S.; Thomsen, D.R. Global Elemental Maps of the Moon: The Lunar Prospector Gamma-Ray Spectrometer. *Science* **1998**, *281*, 1484–1489. [CrossRef] [PubMed]
40. Prettyman, T.H.; Hagerty, J.J.; Elphic, R.C.; Feldman, W.C.; Lawrence, D.J.; McKinney, G.W.; Vaniman, D.T. Elemental composition of the lunar surface: Analysis of gamma ray spectroscopy data from Lunar Prospector. *J. Geophys. Res. Earth Surf.* **2006**, *111*, E12007. [CrossRef]
41. Elphic, R.C.; Lawrence, D.J.; Feldman, W.C.; Barraclough, B.L.; Maurice, S.; Binder, A.B.; Lucey, P.G. Lunar rare earth element distribution and ramifications for FeO and TiO_2: Lunar Prospector neutron spectrometer observations. *J. Geophys. Res. Earth Surf.* **2000**, *105*, 20333–20345. [CrossRef]

42. Heiken, G.H.; Vaniman, D.T.; French, B.M. Lunar Chemistry. In *Lunar Sourcebook, a User's Guide to the Moon*; Cambridge University Press: Cambridge, UK, 1991; Chapter 8; pp. 357–474.
43. Grumpe, A.; Belkhir, F.; Wöhler, C. Construction of lunar DEMs based on reflectance modelling. *Adv. Space Res.* **2014**, *53*, 1735–1767. [CrossRef]
44. Scholten, F.; Oberst, J.; Matz, K.-D.; Roatsch, T.; Wahlisch, M.; Speyerer, E.; Robinson, M.S. GLD100: The near-global lunar 100 m raster DTM from LROC WAC stereo image data. *J. Geophys. Res. Earth Surf.* **2012**, *117*, E00H17. [CrossRef]
45. Hapke, B. Bidirectional reflectance spectroscopy: 3. Correction for macroscopic roughness. *Icarus* **1984**, *59*, 41–59. [CrossRef]
46. Hapke, B. Bidirectional Reflectance Spectroscopy: 5. The Coherent Backscatter Opposition Effect and Anisotropic Scattering. *Icarus* **2002**, *157*, 523–534. [CrossRef]
47. Wöhler, C.; Berezhnoy, A.; Evans, R. Estimation of elemental abundances of the lunar regolith using clementine UVVIS+NIR data. *Planet. Space Sci.* **2011**, *59*, 92–110. [CrossRef]
48. Öhman, T.; Kramer, G.Y.; Kring, D.A. Characterization of melt and ejecta deposits of Kepler crater from remote sensing data. *J. Geophys. Res. Planets* **2014**, *119*, 1238–1258. [CrossRef]
49. Grumpe, A.; Wöhler, C.; Berezhnoy, A.A.; Shevchenko, V.V. Time-of-day-dependent behavior of surficial lunar hydroxyl/water: Observations and modeling. *Icarus* **2018**, *321*, 486–507. [CrossRef]
50. Staid, M.I.; Pieters, C.M.; Besse, S.; Boardman, J.; Dhingra, D.; Green, R.; Head, J.W.; Isaacson, P.; Klima, R.; Kramer, G.; et al. The mineralogy of late stage lunar volcanism as observed by the Moon Mineralogy Mapper on Chandrayaan-1. *J. Geophys. Res. Earth Surf.* **2011**, *116*, E00G10. [CrossRef]
51. Clark, R.N.; Swayze, G.A.; Livo, K.E.; Kokaly, R.F.; Sutley, S.J.; Dalton, J.B.; McDougal, R.R.; Gent, C.A. Imaging spectroscopy: Earth and planetary remote sensing with the USGS Tetracorder and expert systems. *J. Geophys. Res. Planet* **2003**, *108*, 5131. [CrossRef]
52. Adams, J.B. Visible and near-infrared diffuse reflectance spectra of pyroxenes as applied to remote sensing of solid objects in the solar system. *J. Geophys. Res. Earth Surf.* **1974**, *79*, 4829–4836. [CrossRef]
53. Pieters, C.M.; Hanna, K.D.; Cheek, L.; Dhingra, D.; Prissel, T.; Jackson, C.; Moriarty, D.; Parman, S.; Taylor, L.A. The distribution of Mg-spinel across the Moon and constraints on crustal origin. *Am. Miner.* **2014**, *99*, 1893–1910. [CrossRef]
54. Barker, M.; Mazarico, E.; Neumann, G.; Zuber, M.; Haruyama, J.; Smith, D. A new lunar digital elevation model from the Lunar Orbiter Laser Altimeter and SELENE Terrain Camera. *Icarus* **2015**, *273*, 346–355. [CrossRef]
55. Xia, W.; Wang, X.; Zhao, S.; Jin, H.; Chen, X.; Yang, M.; Wu, X.; Hu, C.; Zhang, Y.; Shi, Y.; et al. New maps of lunar surface chemistry. *Icarus* **2018**, *321*, 200–215. [CrossRef]
56. Ohtake, M.; Takeda, H.; Matsunaga, T.; Yokota, Y.; Haruyama, J.; Morota, T.; Yamamoto, S.; Ogawa, Y.; Hiroi, T.; Karouji, Y.; et al. Asymmetric crustal growth on the Moon indicated by primitive farside highland materials. *Nat. Geosci.* **2012**, *5*, 384–388. [CrossRef]
57. Souchon, A.; Besse, S.; Pinet, P.; Chevrel, S.; Daydou, Y.; Josset, J.-L.; D'Uston, L.; Haruyama, J. Local spectrophotometric properties of pyroclastic deposits at the Lavoisier lunar crater. *Icarus* **2013**, *225*, 1–14. [CrossRef]
58. Pieters, C.M.; Besse, S.; Boardman, J.; Buratti, B.; Cheek, L.; Clark, R.N.; Combe, J.P.; Dhingra, D.; Goswami, J.N.; Green, R.O.; et al. Mg-spinel lithology: A new rock type on the lunar farside. *J. Geophys. Res. Earth Surf.* **2011**, *116*, E00G08. [CrossRef]
59. Yamamoto, S.; Nakamura, R.; Matsunaga, T.; Ogawa, Y.; Ishihara, Y.; Morota, T.; Hirata, N.; Ohtake, M.; Hiroi, T.; Yokota, Y.; et al. A new type of pyroclastic deposit on the Moon containing Fe-spinel and chromite. *Geophys. Res. Lett.* **2013**, *40*, 4549–4554. [CrossRef]
60. Sivakumar, V.; Neelakantan, R. Reflectance Imaging Spectroscopy Data (Hyperspectral) for Mineral Mapping in the Orientale Basin Region on the Moon Surface. *Int. J. Geol. Environ. Eng.* **2016**, *10*, 303–306.
61. Thesniya, P.; Rajesh, V. Pyroxene chemistry and crystallization history of basaltic units in the Mare Humorum on the nearside of the Moon: Implications for the volcanic history of the region. *Planet. Space Sci.* **2020**, *193*, 105093. [CrossRef]
62. Ling, Z.; Zhang, J.; Liu, J.; Zhang, W.; Zhang, G.; Liu, B.; Ren, X.; Mu, L.; Liu, J.; Li, C. Preliminary results of TiO_2 mapping using Imaging Interferometer data from Chang'E-1. *Chin. Sci. Bull.* **2011**, *56*, 2082–2087. [CrossRef]
63. Lemelin, M.; Morisset, C.-E.; Germain, M.; Hipkin, V.; Goïta, K.; Lucey, P.G. Ilmenite mapping of the lunar regolith over Mare Australe and Mare Ingenii regions: An optimized multisource approach based on Hapke radiative transfer theory. *J. Geophys. Res. Planets* **2013**, *118*, 2582–2593. [CrossRef]
64. He, Z.P.; Wang, B.Y.; Lv, G.; Li, C.L.; Yuan, L.Y.; Xu, R.; Chen, K.; Wang, J.Y. Visible and near-infrared imaging spectrometer and its preliminary results from the Chang'E 3 project. *Rev. Sci. Instrum.* **2014**, *85*, 083104. [CrossRef]
65. Coombs, C.R.; Hawke, B.R.; Robinson, M.S. Pyroclastic deposits on the northwestern limb of the Moon. In Proceedings of the Lunar and Planetary Science Conference, Houston, TX, USA, 16–20 March 1992; Volume 23.
66. Head, J.W.; Wilson, L. Rethinking Lunar Mare Basalt Regolith Formation: New Concepts of Lava Flow Protolith and Evolution of Regolith Thickness and Internal Structure. *Geophys. Res. Lett.* **2020**, *47*, e2020GL088334. [CrossRef]
67. Sun, Y.; Li, L.; Zhang, Y. Detection of Mg-spinel bearing central peaks using M 3 images: Implications for the petrogenesis of Mg-spinel. *Earth Planet. Sci. Lett.* **2017**, *465*, 48–58. [CrossRef]
68. Isaacson, P.J.; Pieters, C.M. Northern Imbrium Noritic Anomaly. *J. Geophys. Res. Earth Surf.* **2009**, *114*, 09007. [CrossRef]
69. Spudis, P.D. *The Geology of Multi-Ring Impact Basins*; Cambridge University Press: Cambridge, UK, 1993. [CrossRef]
70. Wöhler, C.; Lena, R. Lunar intrusive domes: Morphometric analysis and laccolith modelling. *Icarus* **2009**, *204*, 381–398. [CrossRef]

71. Trang, D.; Gillis-Davis, J.J.; Hawke, B.R. The origin of lunar concentric craters. *Icarus* **2016**, *278*, 62–78. [CrossRef]
72. Liu, T.; Michael, G.; Engelmann, J.; Wünnemann, K.; Oberst, J. Regolith mixing by impacts: Lateral diffusion of basin melt. *Icarus* **2018**, *321*, 691–704. [CrossRef]